Anno Accademico 2007-2008



UNIVERSITÀ DEGLI STUDI DI TRIESTE

FACOLTÀ DI SCIENZE MATEMATICHE, FISICHE E NATURALI
CORSO DI LAUREA SPECIALISTICA IN FISICA

Curriculum: Fisica della Materia

Misure preliminari dalla componente radiale di spin degli stati di superficie di Shockley dell'Au(111)

Relatore:
Ch.mo Prof. Fulvio Parmigiani

Laureando:
Sergio Vlaic

Correlatore:
Dott. Cephise Cacho

Anno Accademico 2007-2008



UNIVERSITÀ DEGLI STUDI DI TRIESTE

FACOLTÀ DI SCIENZE MATEMATICHE, FISICHE E NATURALI
CORSO DI LAUREA SPECIALISTICA IN FISICA

Curriculum: Fisica della Materia

Preliminary measurements of the spin-radial component of the Au(111) Shockley surface states

Relatore:
Ch.mo Prof. Fulvio Parmigiani

Laureando:
Sergio Vlaic

Correlatore:
Dott. Cephise Cacho

Abstract

La presente tesi riporta lo studio sugli stati di superficie dell'Au(111) mediante fotoemissione risolta in angolo e spin. Tali stati presentano un accoppiamento spin-orbita che risolve la degenerazione di spin. Da modelli teorici e calcoli di DFT è noto che, considerando livelli isoenergetici della proiezione del reticolo reciproco sulla superficie, i due stati si dispongono secondo cerchi concentrici (centrati al punto Γ). La componente tangeziale (rispetto a tali cerchi) della polarizzazione di spin risulta totale ed opposta per i due stati; mentre vi è una leggera polarizzazione nella direzione radiale uguale in segno ma diversa in modulo tra i due stati. Questo studio è stato condotto utilizzando come sorgente la quarta armonica di un laser Ti:Sa amplificato ed un Time-of-Flight per la misura dell'energia cinetica degli elettroni. Mediante un Mott-detector con quattro rilevatori viene risolto lo spin. La presenza di quattro rilevatori disposti a 90° uno rispetto all'altro consente di risolvere lo spin nel piano della superficie del campione, quindi per entrambe le componenti: radiale e tangenziale. E' inoltre presentata una procedura per la caratterizzazione del Mott-detector e l'ottimizzazione dei suoi parametri utilizzando le informazioni note sulla componente tangenziale di spin degli stati di superficie.

Index.

Abstract III

Index IV

1. Introduction 1

1.1 Surface states at metal surface. 4

1.2 Spin-orbit coupling in a 2-D electron gas (Rashba–Byckhov model). 9

1.3 State of art. 12

1.4 Scope of the experiment. 16

2. Experimental set-up 17

2.1 Laser system and the 4^{th} harmonic generation (4HG). 18

2.2 The electron Time-of-Flight spectrometer and the spin-detector. 20
2.3 The electron Time-of-Flight (ToF) spectrometer. 22
2.4 Principle of the Mott-polarimeter. 24
2.5 Time and energy resolution. 32

3. The Mott-detector and ToF calibrations 35

3.1 Conversion of the raw data in the spin data. 36
3.2 Self calibration of the energy dispersion curve (EDC) to extract the experimental asymmetry and the Sherman function. 40
3.3 Sherman function versus the Mott-polarimeter high voltage scattering. 45

4. Spin resolved photoemission from the Au(111) surface states 49

4.1 Angular dispersion of the surface states. 50
4.2 Attempt to measure the radial component. 56

5. Conclusion 60

Bibliography 63

Introduction

Surface states of noble metals are known since Shockley discovered them in 1939 [1] by considering a semi-infinite crystal with a periodic potential. He studied the wave functions of the states with a finite 1-D periodic potential discovering that in the "forbidden" region between the allowed bands some occupied surface states should be expected. Today we know that, in a more complex 3-D picture, these states give rise to surface bands. They originate from electrons trapped between the surface step potential of the crystal and the bulk potential [2]. Therefore, surface states, that are predicted for all metals, play an important role in determining the surface or interface properties and process, such adsorption, catalysis and, therewith, chemical reactions at surfaces [3].

Recently it turned out that the surface states on the (111) surface of noble metals show an energy splitting due to spin-orbit coupling [4]. The spin-orbit splitting is a quite common mechanism in semiconductor heterojunctions, where a two-dimensional electron gas is created [5]. The asymmetry at these interfaces gives rise to the *Rashba-Bychkov* interaction [6]-[7] which leads to the spin-orbit splitting and to the spin polarization of the free-electron like-states at the interface. At the (111) surface of noble metals the mechanism is

similar and an energy splitting of the surface states due to the *Rashba-Bychkov* interaction is observed [8]. In this case the surface breaks the inversion symmetry in the direction normal to the surface, while the spin-orbit interaction lifts the spin degeneracy, providing different energies for the two spin states at given values of the reciprocal momentum vector.

In the last few years some scholars started to study the surface states of noble metals using the spin resolved photoemission spectroscopy [8], [9], obtaining a direct observation of the spin polarization of the surface states.

In this thesis the Au(111) surface states are investigated by coherent low photon energy angle resolved photoelectron spectroscopy (ARPES) using a Mott-detector to resolve the spin state of the photoemitted electrons, the purpose being the absolute calibration of the Mott-detector and the spin-resolved dispersion of the surface states. The Mott-polarimeter is based on the spin-orbit interaction between the photoelectrons and the Au atoms of a foil placed at the centre of the detector. To obtain the best spin sensitive condition the photoelectrons are accelerated by an electrostatic potential. The spin sensitivity of the detector is analyzed as a function of this accelerating potential in order to define the operating conditions.

The spin resolved energy dispersions are also obtained finding, in the momentum space, the parabolic behaviour of the two surface states as a function of the component parallel to the surface of the reciprocal momentum vector. The isoenergetic curves in the reciprocal lattice of Au(111) surface states, at given binding energy values, are composed by two concentric circles separated by the energy contribution due to the spin-orbit coupling (Fig 1.1).

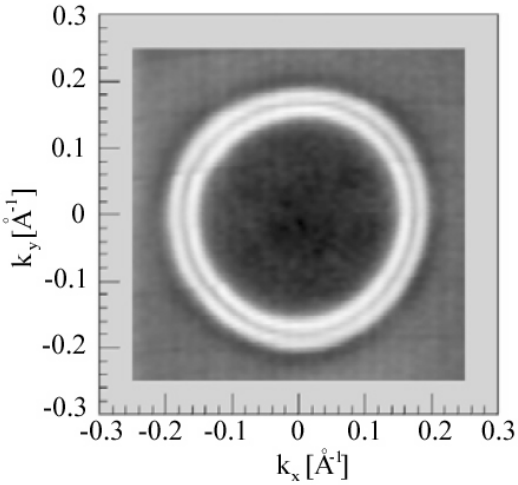


Fig 1.1 Isoenergetic curve in the reciprocal lattice of the Au(111) surface states. The two rings are separated by the spin-orbit energy contribution. Deviations from a perfect circular shape are due to experimental effect. [4]

Density functional theory (DFT) calculations [8] show that in the tangential direction, the surface states should be fully polarized with opposite spin directions. In the radial direction the spin polarization is very small and it should have the same sign for the two but changing sign every 60 deg in the surface plane.

Here it is shown that the tangential spin component resulting from LDA calculation is consistent with our measurements, whereas for the radial component only a first attempt to measure its value is presented.

The thesis is organized as follows

Section 1 reports the relevant physics of the surface states with a short presentation of the Rashba-Bychkov model applied to the surface states of noble metals.

Section 2 describes the experimental apparatus based on an Ti:Sa laser amplifier and a Time-of-Flight electron spectrometer equipped with a spin-polarimeter.

Section 3 presents the data analysis, in particular how to extract the spin data from the detected spectra, along with the fitting procedure and the characterization of the spin detector.
Section 4 shows the results, the energy dispersion of the Au(111) surface states.
The last section reports the conclusion.

1.1 Surface states at metal surface

The conventional approach for describing a solids starts from an infinite crystal with a full translation symmetry. However, real crystals present many brake-downs of the periodicity and local defects. The surface originates from the interruption of the translational symmetry and this can be considered the most macroscopic "defects" of an ideal crystal. For this reason at the solid surfaces many physical and chemical phenomena take place and among them the surface states.
The surface states are spatially confined at the surface region. Inside the crystal the real part of the wave function is modulated by a *sine* or *cosine* function.
The origin of these states is sketched by the simple model reported in Fig 1.2 [10]. This model assumes a constant potential inside the solid, while the surface is represented by a step potential (Fig 1.2(a)). In such a model the wave function which amplitude decay exponentially outside the crystal while inside the crystal it is represented by a travelling wave with real $\bar{k}$-vector. As a consequence in a free-electron-gas model with a step-like surface potential the surface states do not exist, since every energy corresponds to a constant amplitude travelling wave.

If the crystal lattice is represented by a weak periodic potential (nearly-free-electron model) with a step termination at the surface

$$V(z) = V_0 + 2V\cos\frac{2\pi}{a}z \qquad z>0 \qquad (1.1)$$

being *z* the coordinate perpendicular to the surface and *a* the lattice parameter in the *z* direction and $V_0 \approx 0$.

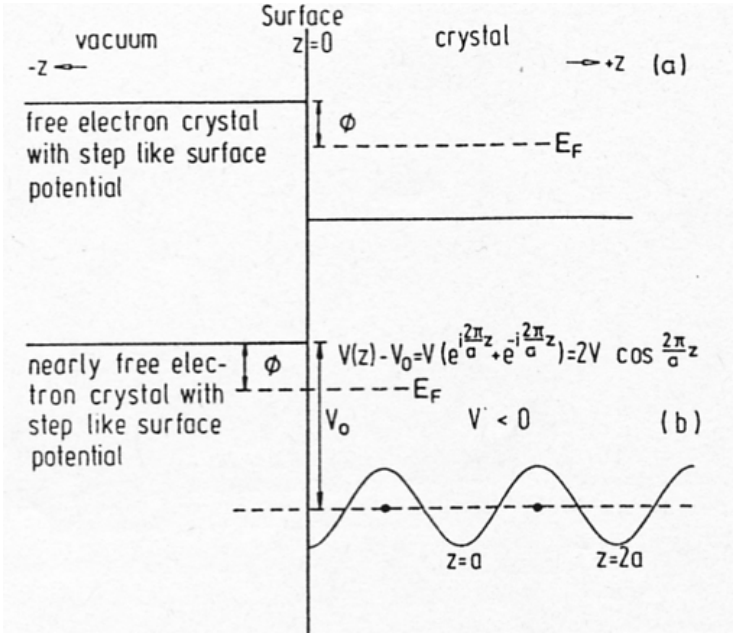


Fig 1.1. Representation of the surface of a crystal. (a) Free electron crystal with a step-like surface potential. (b) Nearly-free-electron solid with a potential: $V(z) = 2V_g \cos(2\pi/a)z$ with *V<0*. The origin is taken between the ions core.

The sign of *V* depends on the position of the origin [see Fig 1.2(b)]. In Fig 1.2(b) the origin is set between the ions. The potential *V(z)* modifies the free electron band structure in such a way that a gap at the boundary of the Brillouin zone ($k_z = \pm \pi/a, \pm 2\pi/a, ...$) opens [11].

The one-dimensional Schrödinger equation is:

$$\frac{\hbar^2}{2m}\frac{d^2\psi(z)}{dz^2}+[E-V(z)]\psi(z)=0. \qquad (1.2)$$

The solutions near the boundary of the Brillouin zone have the following form:

$$\psi(z)=A\exp(ik_z z)+B\exp(ik_z z-ig_z z) \qquad (1.3)$$

where $k_z=\pm\pi/a$ and $g_z=2\pi/a$ (In the following only the point $k_z=\pi/a$ will be considered) and *A* and *B* are the normalization's constants.

The wave function at the bottom and at the top of the gap has the following form:

V<0: *top* $\psi\approx\cos(\frac{\pi}{a}z)$ *s-type*

Bottom $\psi\approx\cos(\frac{\pi}{a}z-\frac{\pi}{a})\approx\sin(\frac{\pi}{a}z)$ *p-type*

This solution can be extended into the gap by using a complex $\bar{k}$-vector: $k_z=p\pm iq$ with $p=\pi/a$ and $q\in R$ in order to have a solution near the Brillouin boundary.

The wave functions become:

$$\psi(z)=e^{i(p\pm iq)z}(A+Be^{-igz})=e^{\mp qz}e^{ipz}(A+Be^{-igz}) \qquad (1.4)$$

In an infinite crystal both solutions are forbidden since the first exponential diverges for $z\to-\infty$ and $z\to+\infty$, but for the situation chosen (a crystal extending to $+\infty$) the wave function $\psi(z)=e^{-qz}e^{ipz}(A+Be^{-igz})$ is a possible solution since it decays into the crystal.

By setting $A=e^{i\delta}$ and $B=e^{-i\delta}$ with $\delta\in R$. The following wave function is obtained,

$$\psi=Ce^{-qz}\cos(\frac{\pi}{a}z+\delta) \qquad \text{(for } z>0\text{)} \qquad (1.6)$$

where (for q>0) δ is

$\delta=0$ *Top*

$\delta=-\pi/2$ *Bottom*

The wave function outside the crystal decays exponentially

$$\psi = De^{q'z} \quad \text{(for z<0).} \qquad (1.7)$$

The coefficients *C* and *D* are found from the matching between the wave function and its derivate at the surface of the crystal (*z=0*). Toward the vacuum the derivative of the wave function is given by

$$\left.\frac{d\psi}{dz}\right|_{z=0} = Dq'e^{q'z}\Big|_{z=0} = Dq' > 0 \qquad (1.8)$$

while toward the crystal at the bottom of the gap ($-\pi/2$) is

$$\left.\frac{d\psi}{dz}\right|_{z=0} = Cp[-\sin(-\pi/2)] > 0 \qquad (1.9)$$

Eq 1.8 and eq 1.9 show that a matching between the derivates is possible.

Moreover, at the surface it is possible to match, the wave function inside and outside the crystal. Nontheless, the matching is not possible for $\delta=-\pi/2$ since the inner wave function is zero at the surface and for $\delta=0$ since the derivates cannot be matched. Otherwise for $-\pi/2<\delta<0$ there is a region where the matching is possible and surface states can exist.

Another way to look at the matching conditions is to use the logarithmic derivate that is the ratio between the derivative of the wave function and the wave function: $\left.\frac{d\psi}{dz}/\psi\right|_{out} = \left.\frac{d\psi}{dz}/\psi\right|_{in}$ and therefore

$$q' = -q - p\tan\delta \qquad (1.10)$$

The physical meaning of eq 1.10 resides in the fact that to describe an electron in a gap a complex wave vector ($k=p+iq$) must be considered. In this case the resulting wave functions have real exponents *[exp(qz)]*. The real exponent

wave functions are forbidden for an infinite crystal (since they diverge as $z \to \pm\infty$) but for a semi-infinite crystal there are exponentially decaying wave functions outside and inside the crystal. This leads to states confined at the surface.

Fig 1.3 shows the Fermi surface of the gold and the projection of the bulk Brillouin zone to the surface Brillouin zone ($\pm 0.8\ \AA^{-1}$).

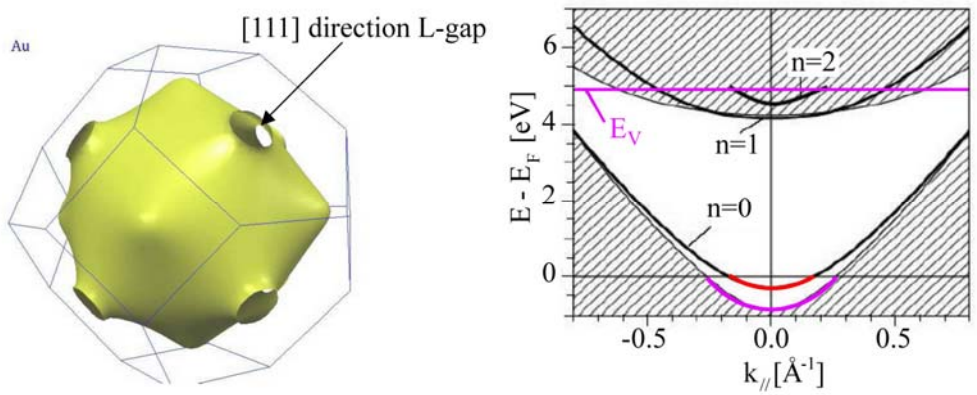


Fig 1.3. Left panel: Au Fermi surface representation.
Right panel: Projection of the bulk Brillouin zone of the gold to the surface Brillouin zone [12]

In the [111] direction the band structure of Au presents a band gap (Fig 1.3 left panel). This band gap is quite evident in the momentum domain around $\Gamma(\bar{k} = 0)$ by projecting the bulk Brillouin zone on to the surface. This is the typical condition for the formation of the surface states, since there an electron can be trapped between the band gap and the vacuum level, as shown in Fig 1.3. The binding energy of these states (related to the Fermi energy) is less than 1 eV (Fig 1.3).

1.2 Spin orbit coupling in a 2-D electron gas (Rashba–Byckhov model).

Recently it has been shown that surface states at the (111) surface of noble metals exhibit a spin-orbit interaction with a strong analogy with the two-dimensional electron gas in a semiconductor heterojunctions [4].

The non-relativistic Hamilton operator for electrons with spin-orbit coupling is given by [13]

$$H = \frac{1}{2} p^2 + V(r) + \frac{1}{2c^2} \sigma \bullet [\nabla V(r) \times p] \qquad (1.19)$$

where σ are the Pauli matrices and $p = -i\nabla$ is the momentum operator in atomic units. In order to have a two-dimensional electron gas the potential *V* must confine the electrons in a plane. By choosing the plane orthogonal to *z=0* and setting *V(0)=0* the Hamiltonian becomes:

$$H = \frac{1}{2}(\partial_x^2 + \partial_y^2) + i \frac{\partial_z V(z)\big|_{z=0}}{2c^2} (\sigma_x \partial_y - \sigma_y \partial_x) \qquad (1.20)$$

The ansatz for the eigenfunctions ψ_k is that they consist in plane-wave spinors

$$\psi_k = (\mu_k \chi^+ + \nu_k \chi^-) e^{i(k_x x + k_y y)} \qquad (1.21)$$

with $k = (k_x, k_y)$. The Pauli spinors are quantized with respect to the *z*-axis ($\sigma_z \chi^\pm = \pm \chi^\pm$). From the fact that $\sigma_x \chi^\pm = \chi^\mp$ and $\sigma_y \chi^\pm = \pm i \chi^\mp$ the Schrödinger equation $H\psi_k = E(k)\psi_k$ leads to

$$(k_x + ik_y)\nu_k^2 = (k_y - ik_x)\mu_k^2 \qquad (1.22)$$

The normalization of ψ_k gives the conditions for the two sets of coefficients (index + or -):

$$\mu_{k\pm} = \frac{1}{\sqrt{2}}, \qquad \nu_{k\pm} = \mp \frac{1}{\sqrt{2}} \sqrt{\frac{k_y - ik_x}{k_y + ik_x}} \quad \text{for} \quad k \neq 0 \qquad (1.23)$$

The eigenvalues of ψ_k are given by

$$E_{\pm}(\mathbf{k}) = \frac{1}{2}k^2 \pm \gamma|k| \qquad (1.24)$$

where $\gamma = \partial_z V(z)\big|_{z=0} /(2c^2)$. Therefore, the strength of the spin-orbit splitting is $E_+(k) - E_-(k) = 2\gamma$, hence proportional to the asymmetry given by $\partial_z V(z)$. In this frame the spin polarization $P_{\pm}(\mathbf{k}) = \psi_{\pm}^{*}\sigma\psi_{\pm}$ is complete and perpendicular to k_z,

$$P_{\pm}^{x}(\mathbf{k}) = \mp\frac{k_y}{|\mathbf{k}|}, \qquad P_{\pm}^{y}(\mathbf{k}) = \pm\frac{k_x}{|\mathbf{k}|}, \qquad P_{\pm}^{z}(\mathbf{k}) = 0 \qquad (1.25)$$

Hence, $\mathbf{P}_+(\mathbf{P}_-)$ rotate anticlockwise (clockwise) around the *z*-axis.

For the surface states of a (111) noble metal surface, the electrons are asymmetrically confined at the surface region by the bulk band gap potential and by the surface barrier potential. The spin-orbit coupling is stronger in regions where the crystal potential changes rapidly ($\partial_z V(z)$). Therefore, for this reason, is more evident in heavy atoms.

Appling the *Rashba-Bychkov* two-dimensional electron gas model to the case of surface states in noble metals the momentum distribution in the reciprocal space consists in two concentric circles separated by 2γ (Fig 1.3)

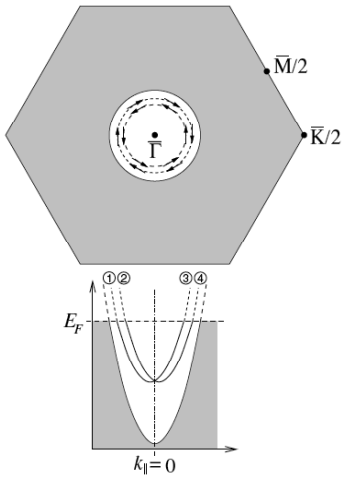


Fig 1.3. Upper panel, section of the SBZ of Au(111) surface. Lower panel, schematic view of the surface states dispersion [4].

The quantity γ reflects the strength of the structural asymmetry and its sign determinates which state is inner ('+' for $\gamma>0$) and which is outer ('-' for $\gamma<0$). This splitting generates fully spin polarized electronic states within the *xy*-plane perpendicular to $\mathbf{k}_{//} = |\mathbf{k}_{//}|(\cos\varphi_e, \sin\varphi_e)$.

$$P_{\pm}^{x(}(\mathbf{k}_{//}) = \alpha_{\pm}\sin\varphi_e, \qquad P_{\pm}^{y}(\mathbf{k}_{//}) = -\alpha_{\pm}\cos\varphi_e, \qquad P_{\pm}^{z}(\mathbf{k}_{//}) = 0$$

with $\alpha_{\pm} = \mp 1$.

$\mathbf{P}_{\pm}$ can be decomposed into a radial and a tangential component by considering the two circles of the momentum distribution

$$P_{\pm}^{rad}(\mathbf{k}_{//}) = P_{\pm}^{x}\cos\varphi_e + P_{\pm}^{y}\sin\varphi_e, \qquad P_{\pm}^{\tan}(\mathbf{k}_{//}) = P_{\pm}^{x}\sin\varphi_e - P_{\pm}^{y}\cos\varphi_e.$$

For this model $P_{\pm}^{rad} = 0$ and $P_{\pm}^{\tan} = \mp 1$ i.e. the radial component is null.

1.3 State of art

The first experimental observation of surface states on noble metals was done in 1975 by Gartlan *et al* [14]. They performed angle resolved photoemission from the Cu (111) surface using a monochromatic light at 6.6 eV. They found two different well separated peaks in the spectra (see Fig 1.5), the first due to the direct transition across the s-p band gap of copper. The second just below the Fermi energy (~0.40eV below at normal emission) was interpreted by an emission from the surface band.

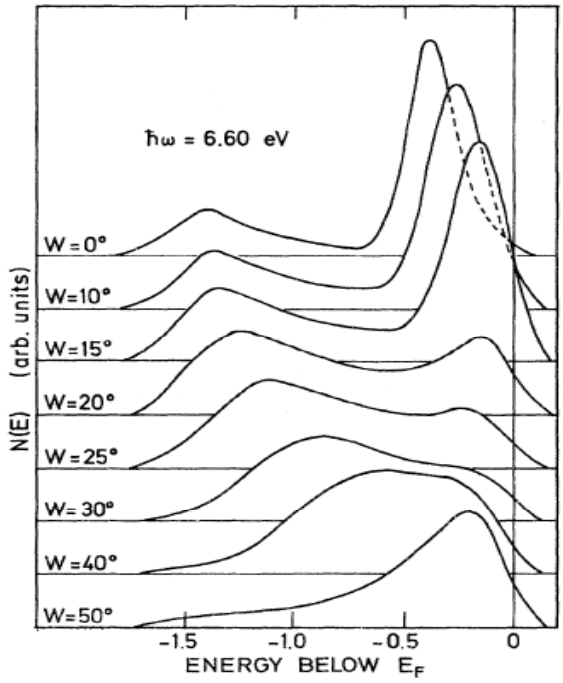


Fig 1.5 Experimental energy distribution curves of photoelectrons emitted at various angles ω relative to the Cu(111) surface. The photon energy is 6.60 eV. [14]

Starting from this experimental evidence many other investigations were performed using angle resolved photoemission in the near UV region [15]–[19].

The first experimental evidence of the spin-orbit splitting of the surface states on a (111) noble metal surface was done by LaShell *et al* [20]. They performed angle resolved photoemission from the Au(111) surface at room temperature using photon energy of $h\nu = 11.83eV$ (Ar I). In this experiment off normal emission, their photoemission spectra showed a line doublet with energy difference that increase linearly with $k_{//}$ (see Fig. 1.6).

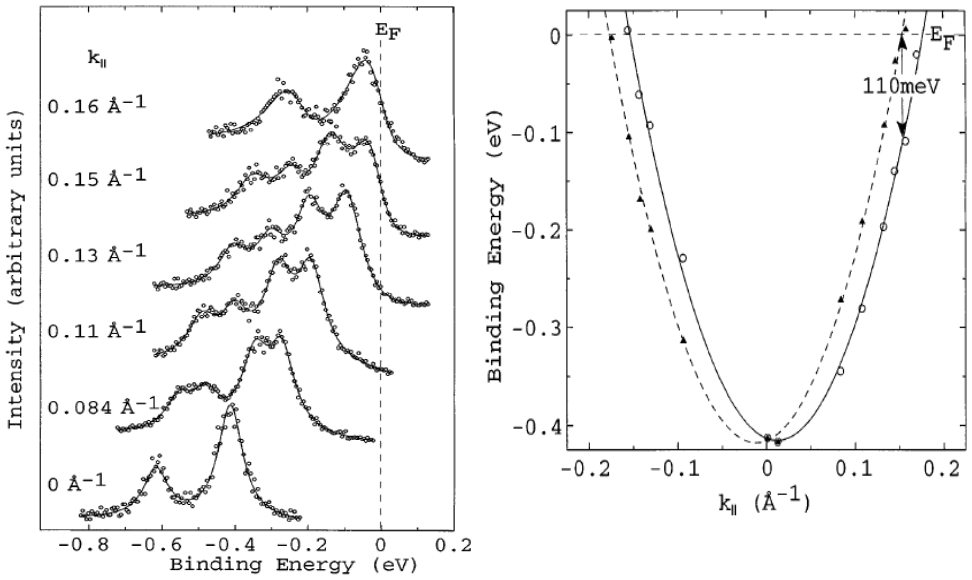


Fig 1.5 Left: spectra taken along the Γ-M direction of the Au(111) reciprocal lattice at the indicated values of parallel momentum with photon energy of $h\nu = 11.83eV$. Along the Γ-M direction is clearly visible a splitting in the first peak which is interpreted as spin-orbit splitting of the surface states. Right: dispersion of the two surface states. [20]

LaShell and co-authors interpreted properly the origin of the two emissions as the spin-orbit splitting of sp-like surface states electrons.

Recently, some theoretical calculations were performed on the surface states of noble metals [4]. Density-functional theory (DFT) calculations showed that the split of the surface states depends on the gradient of the crystal potential

perpendicular to the surface and on the amount of p-character of the states [4]. For the Au(111) surface states the splitting is quite high (on the order of 10^2 meV). However, for metals lighter than Au (Fig 1.7) the spin-orbit splitting is smaller or comparable to the energy resolution of the present days experimental apparatus [4].

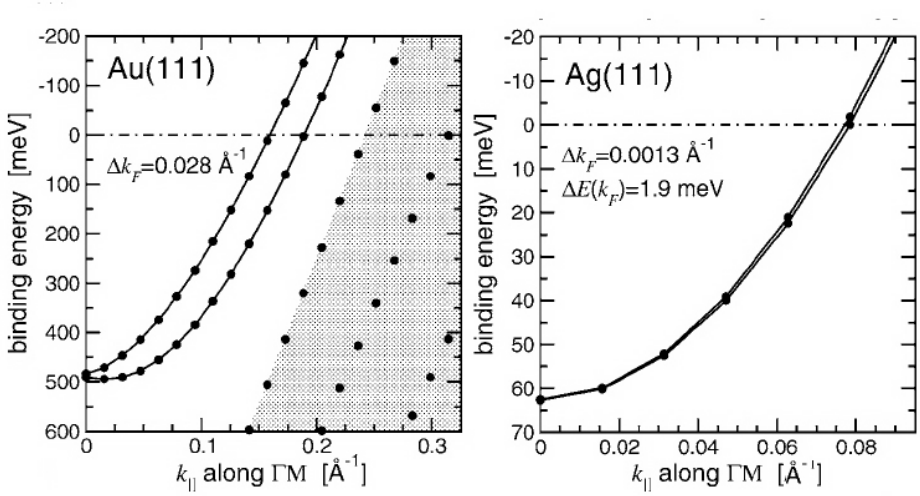


Fig 1.7 Calculated splitting of the Au(111) surface states (left panel) and for the Ag(111) surface states (right panel) [4]

The DFT calculations made on the Au(111) surface states [8] show also that the surface states are also polarized into the radial direction. The radial polarization is very small compared to the tangential component and, so far, has never been observed.

Recently angle and spin resolved photoelectron spectroscopy, using a spin-detector and a hemispherical analyzer, has been applied to study the spin component of the Au(111) surface states [8]. These measurements allow having direct information on the spin polarization of the surface states.

The aim of our experiment is to reach a spin sensitivity suitable for measuring the radial component of the spin polarization on Au(111) surface states. In

2004 Osterwalder *et al* [8] performed spin resolved ARPES on the Au(111) surface states using a $h\nu = 21.1eV$ p-polarized photon source by applying two Mott-detector to a hemispherical analyzer. They also performed DFT calculations deriving the theoretical spectra. The tangential component of the spin polarization was measured finding the theory in consistent agreement with the experiment. However, no data were reported about the radial component.

Fig 1.8 shows their DFT calculations of the spin polarization at 0.17 eV binding energy and the results in the projection of the Brillouin zone to the surface. The solid black lines represent the surface states peaks. The a) panel shows the calculated tangential component of spin polarization of the two surface states. It is possible to see that it is opposite for the two states. The b) panel presents the calculated radial component, that component has the same sign for the two surface states but different values: 6% for the outer surface state, while 2% for the inner one. Moreover the sign of the radial component change every 60 deg in the plane of the surface. The c) panel shows the measured tangential component. The obtained values are in good agreement with the calculated values. It is worthy to note that to perform radial component measurements is useful to rotate the sample in the plane of the surface and detect the 60° modulation.

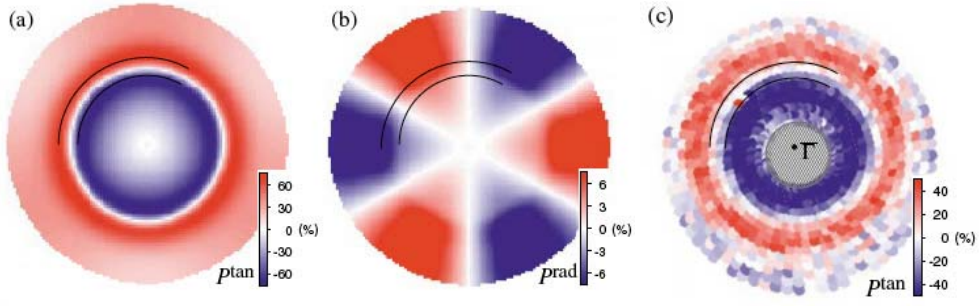


Fig 1.8 Calculated tangential (a) and radial (b) spin-polarization components at 0.17 eV binding energy. The peak position of the surface states is indicated with the black arcs. Measured tangential spin-polarization (c), the radial component was not measured. [8]

1.4 Scope of the experiment

Scope of this work is to test a new system to perform spin and angle photoemission spectroscopy. A Mott-detector, with four micro-channel plates, is applied to a Time-of-Flight electrons analyzer. The light source is the fourth harmonics (~6.2 eV) of a Ti:Sa amplified laser operated at 250 kHz of repetition rate. This apparatus is used for spin resolved ARPES experiment on the Au(111) surface states.

The aims of the experiment are

1. to make use of the fully spin-polarized photoelectron emission of the Au(111) surface state to measure the experimental asymmetry and the Sherman function of the Mott-polarimeter avoiding any magnetic field.
2. to obtain spin-resolved spectra of the Au(111) surface states with an unprecedent resolution.
3. to measure the radial component of the spin polarization.

Experimental set-up

This section reports the description of the experimental set-up. The first part describes the light source used and the optical elements used to generate the fourth harmonics of the laser pulse; the second part describes the Time-of-Flight electron spectrometer and the Mott-detector.

2.1 Laser system and the 4th harmonic generation (4HG).

The light source is based on a Ti-sapphire laser amplifier. Fig 2.1 reports a schematic view of the source. It is composed by a laser pump (Verdi V18), a master oscillator (Mira 900), an amplifier (RegA) and a stretcher-compressor system.

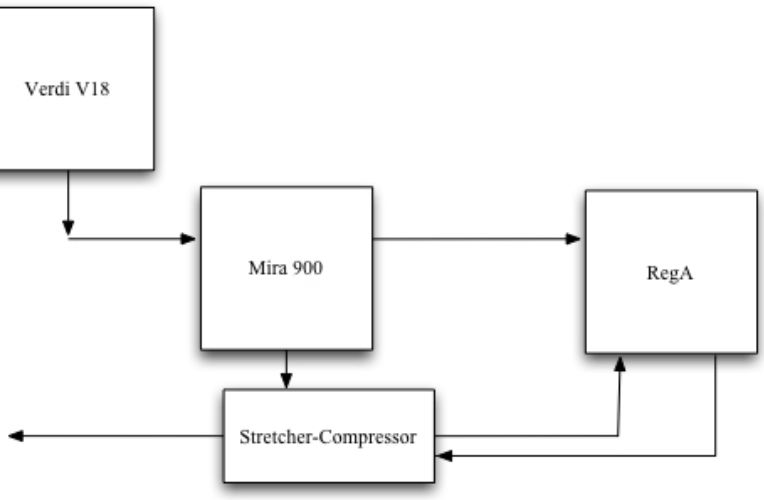


Fig 2.1. Schematic view of the laser source.

The continuous laser light (16 W) emitted by pump (Verdi V18) is splitted into 2 beams inside master oscillator (Mira). The first beam (4.5 W) is used to generate the pulse inside the master oscillator and the second beam (11.5 W) is used to pump the laser amplifier. The output from the oscillator are laser pulses with a wavelength of ~800 nm, and a bandwidth of ~45 nm. The repetition rate is ~83 MHz with an average power of ~550 mW. Downstream this beam is stretched and sent to the laser amplifier, after the amplification the light pulse

is compressed back to the original time-structure. The overall output is a pulse with a wavelength of ~800 nm, a bandwidth of ~30nm, at a repetition rate at ~250 kHz with an average power of ~1.3 W and a pulse duration of ~80 fs. This beam is sent to a series of optical elements (Fig 2.2) to generate the fourth harmonic *i.e.* a pulse at ~200 nm.

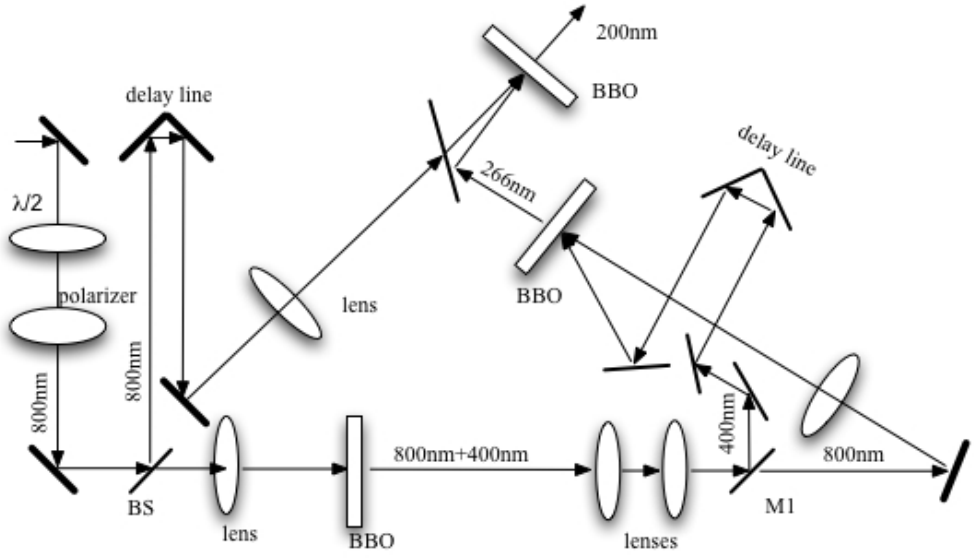


Fig 2.2. Schematic view of the set-up used to generate the fourth harmonic.

The 800 nm beam polarization is rotated from horizontal to vertical direction by a polarizer and then is splitted by a beam splitter (BS in Fig 2.2). One part is used to generate the second harmonic (400 nm) passing through a beta-BaB_2O_4 crystal (BBO) while the other beam follows a different path. After the BBO crystal the overall, 800 nm and 400 nm beams are separated by a dichroic mirror (M1) that transmits the 800 nm and reflects the second harmonic. The two beams are then focalized into a second BBO crystal to generate the third harmonic (266 nm). The 800 nm and 266 nm beams are then focalized out a third BBO crystal to generate the p-polarized fourth harmonic (200 nm). This

beam is focalized on the sample. The beam energy of the fourth harmonic, controlled by a λ/2 plastic set on the entrance beam, is ~5 pJ.

2.2 The Time-of-Flight electron spectrometer and the spin-detector.

The 200 nm pulse is used to emit the photoelectron from the surface states of an Au(111) single crystal. The sample was cleaned with the standard procedure [21], *i.e.* a number of cycles of argon-ion sputtering and annealing at ~500°C. A Time-of-Flight electron analyzer equipped with a Mott-detector (Fig 2.3) is used to measure the electron's kinetic energy and the spin polarization of the photoelectrons.

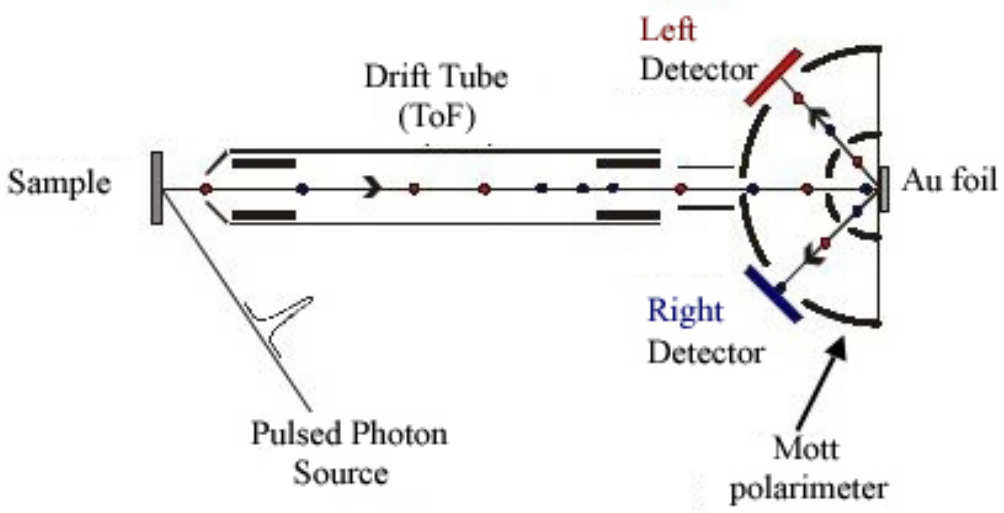


Fig 2.3 Schematic view of the Time-of-Flight Mott-detector.

The ToF consists in a 45 cm drift tube with a small angle of acceptance (±0.15°) in which is possible to put an opposite potential to decelerate the collected electrons (up to 1 kV). After this linear path the electrons enter in the Mott-detector. This detector consists in two hemispheres with five small holes each kept with a differential potential between 10 kV up to 30 kV.

The electrons enter into the detector trough one of the holes to reach the gold foil placed at the centre of the sphere. Some of the electrons are then back elastic-scattered by the gold foil atoms onto to the four microchannel plates placed at the end of the external sphere, as shown in Fig 2.3, passing trough the other four holes. The potential between the two hemispheres accelerates the incoming electrons whereas the back-scattered electrons are decelerated. In the following the Mott-scattering mechanism will be discussed with some details.

2.3 The electron Time-of-Flight spectrometer

The principle of the Time-of-Flight techniques applied to photoemission experiments is to measure the kinetic energy of the electrons by measuring the time needed to cover a fixed distance through a drift tube placed between the sample and the detector. This electron spectrometer is ideal when the photoelectrons are emitted by a pulsed light source [22] since the entire photoelectrons spectral range can be measured at once with an unprecedent energy resolution.

When the pulse is emitted by the source a clock starts and it stops when the electrons hit one of the detectors. Knowing the electrons travelling distance it is possible to calculate the electron kinetic energy. By increasing the length of the drift tube, the time distance between two electrons with different velocity also increases and so does the energy resolution. On the other hand, it is important that the electrons from different bunches do not overlap. Therefore, the tube must be long enough to achieve the desired energy resolution but avoiding the signals overlapping coming from electrons of different bunches.

In practice, the resolution is limited by all the physical effects that can modify the electron trajectories, such as background electric fields and magnetic fields.

Another important difference between the ToF and the conventional electrons analyzers must be considered since for constant energy time and energy have a non-linear relationship, the resolution is not constant over the energy range. In particular, the time-energy relation is expressed by $\Delta E / E = (2\Delta t / t)$ [23], where t is the time of flying electrons t and E is the kinetic energy of the electrons. Fig 2.4 shows the electron Time-of-Flight spectrometer

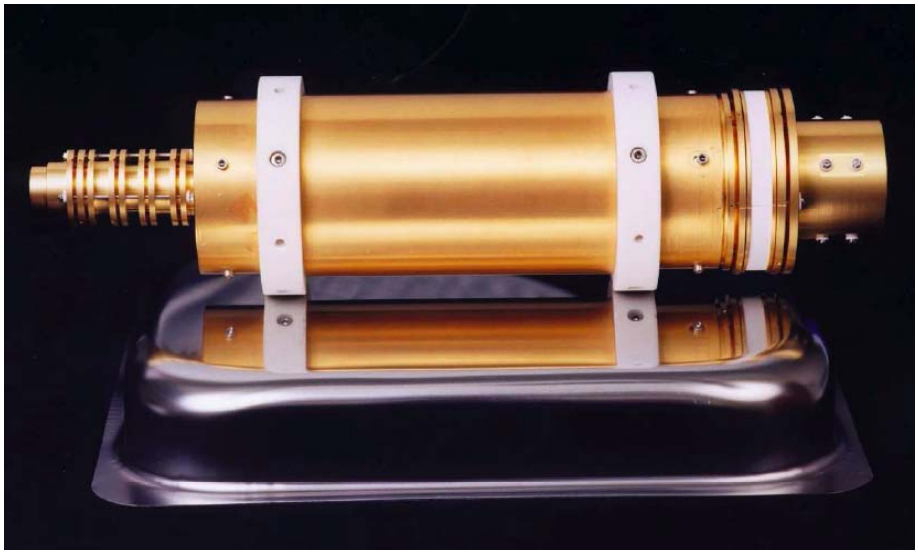


Fig 2.4. The electron Time-of-Flight spectrometer.

2.4 Principle of the Mott-polarimeter

The Mott-polarimeter consists of two hemispheres kept a different potential, a gold foil at the centre and four microchannel plates to detect the photoelectrons.



Fig 2.4 The Mott-detector

The physical principle of the spin detector is based on the so-called Mott-scattering process. This scattering process describes the interaction between an energetic electron and the spin-orbit split electrons of a deep core level of a heavy atom (in our case Au). The probability of back elastic scattering depends on the spin of the incident electrons. In order to maximize this scattering the photoelectrons are accelerated by the potential difference (~25 kV) between the two hemispheres to reach the maximum asymmetry in the scattering probability.

A time-to-digital converter with a 120 ps time of digitalization measures the arrival time on the four detectors. The measured time is after converted into kinetic energy.

In the following, the Mott-scattering process is described by considering the case of one electron and one scattering centre. To show the spin dependent scattering probability it is necessary to calculate the differential cross section of the scattering process using the Dirac equation in the presence of an external field. The process consists in scattering by relativistic electrons with spin by a central field, so the equation is [24]-[25]:

$$\left[\frac{1}{2m}\left(\bar{p}-\frac{e}{c}\bar{A}\right)^2+e\Phi-\frac{e\hbar}{2mc}\bar{\sigma}\bullet\bar{B}+i\frac{e\hbar}{4m^2c^2}\bar{E}\bullet\bar{p}-\frac{e\hbar}{4m^2c^2}\bar{\sigma}\bullet(\bar{E}\times\bar{p})\right]\psi=W\psi \tag{2.1}$$

where $\bar{p}$ is the momentum operator, m is the electron mass, c is the speed of light, $\bar{A}$ is the vector potential, e is the electron charge, ϕ is the electric potential, $\bar{\sigma}$ is the Pauli operator, $\bar{B}$ is the magnetic field, $\bar{E}$ is the electric field and $W+mc^2$ is the total energy.

The first two terms are identical to the Schrödinger equation for external fields. The third term represents the interaction between the magnetic dipole and the magnetic external field. The fourth term is a relativistic correction to the energy and has no classical analogue. The last term is the spin-orbit operator and is the relevant part of the Hamiltonian that describes the Mott-scattering. If the external field has a spherical symmetry

$$E=-e^{-1}(dV/dr)(\bar{r}/r) \tag{2.2}$$

the spin orbit term becomes

$$\frac{1}{2m^2c^2}\frac{1}{r}\frac{dV}{dr}(\bar{s}\bullet\bar{l}) \tag{2.3}$$

The incident electron is taken as a plane wave in the *z* direction.

It is important to remember that the relativistic solution for one-dimensional free particle propagating in the *z* direction in the relativistic case which is the generalized plane wave:

$$\left[A\begin{pmatrix} 1 \\ 0 \\ \dfrac{cp_z}{E+mc^2} \\ 0 \end{pmatrix} + B\begin{pmatrix} 0 \\ 1 \\ 0 \\ \dfrac{-cp_z}{E+mc^2} \end{pmatrix} \right] \exp(ikz - i\omega t) \qquad (2.4)$$

The two independent solutions are eigenstates of the Pauli spin operator σ_z, that means

$$\sigma_z \begin{pmatrix} 1 \\ 0 \\ \dfrac{cp_z}{E+mc^2} \\ 0 \end{pmatrix} \exp(ikz) = 1 * \begin{pmatrix} 1 \\ 0 \\ \dfrac{cp_z}{E+mc^2} \\ 0 \end{pmatrix} \exp(ikz) \qquad (2.5)$$

and

$$\sigma_z \begin{pmatrix} 0 \\ 1 \\ 0 \\ \dfrac{-cp_z}{E+mc^2} \end{pmatrix} \exp(ikz) = -1 * \begin{pmatrix} 0 \\ 1 \\ 0 \\ \dfrac{-cp_z}{E+mc^2} \end{pmatrix} \exp(ikz) \qquad (2.6)$$

It is important to notice that this formalism defines the spin polarization components of the electron as

$$P_j = \frac{\langle \psi | \sigma_j | \psi \rangle}{\langle \psi | \psi \rangle} \qquad j = x,y,z \qquad (2.7)$$

In analogy with the non-relativistic case it is necessary to search for solutions of the Dirac equation of the asymptotic form,

$$\psi_\lambda \underset{r \to +\infty}{\rightarrow} a_\lambda \exp(ikz) + a'_\lambda(\vartheta, \phi) \frac{\exp(ikr)}{r} \qquad (2.8)$$

with $\lambda=1,2,3,4$, for the four components of the relativistic wave function, This is equivalent to search for a solution far away from the scattering centre described by the sum of plane wave (unscattered particles) and a spherical wave (scattered particle).

Generalizing the elastic differential cross section obtained with the Schrödinger scattering theory the following differential cross section is obtained

$$\frac{d\sigma}{d\Omega}(\vartheta,\phi)=\frac{\sum_{\lambda=1}^{4}\left|a'_{\lambda}(\vartheta,\phi)\right|^{2}}{\sum_{\lambda=1}^{4}\left|a_{\lambda}\right|^{2}} \qquad (2.9).$$

This follows from the general definition of differential cross section, *i.e.* the ratio between the total probability of scattering and the probability to have an incident electron. Eq 2.8 can be simplified using the relations among the a_λ (see eq 2.5).

$$r=\frac{|a_3|}{|a_1|}=\frac{|a_4|}{|a_2|}=\frac{cp_z}{E+mc^2} \qquad (2.10).$$

The same relation is valid also for the a'_λ coefficients because at very large distance from the scattering centre the spherical wave can be seen as the superposition of plane waves proceeding in different directions. So the differential cross section can be written as,

$$\frac{d\sigma}{d\Omega}(\vartheta,\phi)=\frac{|a'_1|^2+|a'_2|^2}{|a_1|^2+|a_2|^2} \qquad (2.11).$$

For this process it is possible, (see eq 2.10), to take into account only the "large" part of the spinor, so only the first two components of the wave function bring information about the process. Therefore, for an electron travelling in the *z* direction with the spin in the same direction (+*z*) the relevant equation is,

$$\begin{pmatrix}\psi_1\\ \psi_2\end{pmatrix}=\begin{pmatrix}1\\ 0\end{pmatrix}\exp(ikz) \qquad (2.12)$$

and the asymptotic solution is:

$$\begin{pmatrix}\psi_1\\ \psi_2\end{pmatrix}\underset{r\to+\infty}{\longrightarrow}\begin{pmatrix}1\\ 0\end{pmatrix}\exp(ikz)+\begin{pmatrix}S_{11}(\vartheta,\phi)\\ S_{21}(\vartheta,\phi)\end{pmatrix}\frac{\exp(ikr)}{r} \qquad (2.13)$$

After the scattering the second component of the wave function can be different from *0*, hence the spin flip is allowed because of the spin orbit coupling between the electron and the scattering centre. The amplitude of this process is described by S_{21}.

An analogous solution is expected when the electron moves towards the scattering centre with the spin in –*z* direction.

$$\begin{pmatrix}\psi_1\\ \psi_2\end{pmatrix}\underset{r\to+\infty}{\longrightarrow}\begin{pmatrix}0\\ 1\end{pmatrix}\exp(ikz)+\begin{pmatrix}S_{21}(\vartheta,\phi)\\ S_{22}(\vartheta,\phi)\end{pmatrix}\frac{\exp(ikr)}{r} \qquad (2.14)$$

The equations for this problem can be solved using the partial wave method, where a particular solution for a specific angular momentum is considered to build up the general solution (for details see [26]). For an electron with spin along +*z* and separating the variables in the Dirac equation for a central field the two particular independent solutions for a fixed angular momentum l are

$$\begin{pmatrix}\psi_1\\ \psi_2\end{pmatrix}=\begin{pmatrix}(l+1)G_l(r)P_l\cos(\vartheta)\\ G_l(r)P_l^1\cos(\vartheta)e^{i\phi}\end{pmatrix}$$
$$\begin{pmatrix}\psi_1\\ \psi_2\end{pmatrix}=\begin{pmatrix}lG_{-l-1}(r)P_l\cos(\vartheta)\\ G_{-l-1}(r)P_l^1\cos(\vartheta)e^{i\phi}\end{pmatrix} \qquad (2.15)$$

where $P_l(\cos\vartheta)$ are the Legendre functions and ϕ is the azimuth angle. The functions $G_l(r)$ and $G_{-l-1}(r)$ are the solutions obtained for the two radial equations. The reason to have two different solutions can be explained by the spin-orbit coupling term. The spin orbit operator is proportional to $s\bullet l$, so that $\mathbf{l}\bullet\mathbf{s}=\frac{1}{2}(j^2-l^2-s^2)$, while the eigenvalue is $j(j+1)-l(l+1)-s(s+1)$. In this case *s=1/2* for the electron and the angular momentum is fixed, however *j* can have two different values, and the eigenvalues of the spin-orbit term are l, if $j=l+1/2$ or $-l-1$ if $j=l-1/2$. Another important term that appears in these

two solutions is the ϕ angle dependence. Because of the conservation, the component of m_{jz}, which is $m_{jz} = +1/2$ for $l = 0$, becomes $m_{jz} = -1/2$ after the scattering. For a spin-flip described by ψ_2 (eq 2.15), the decrease of the z component of the spin must be compensated by the increase in the angular momentum component l_z, (described by the operator $l_z = -i\hbar\frac{\partial}{\partial\phi}$) therefore the solution must contain a ϕ term.

The general solution is obtained by combining a particular solution with the all possible values of the angular momentum

$$\begin{aligned}\psi_1 &= \sum_{l=0}^{\infty}[(l+1)e^{i\eta_l}G_l + le^{i\eta_{-l-1}}G_{-l-1}]i^l P_l(\cos\vartheta) \\ \psi_1 &= \sum_{l=0}^{\infty}[-e^{i\eta_l}G_l + e^{i\eta_{-l-1}}G_{-l-1}]i^l P_l^1(\cos\vartheta)e^{i\phi}\end{aligned} \tag{2.16}$$

Comparing eq 2.15 and eq 2.16 it is possible to find the conditions required to satisfy the assumption in eq 2.14,

$$\begin{aligned}S_{11}(\vartheta,\phi) &= \frac{1}{2ik}\sum_{l=0}^{\infty}[(l+1)(e^{2i\eta_l}-1) + l(e^{2i\eta_{-l-1}}-1)]P_l(\cos\vartheta) = f(\vartheta) \\ S_{21}(\vartheta,\phi) &= \frac{1}{2ik}\sum_{l=0}^{\infty}[-e^{2i\eta_l} + e^{2i\eta_{-l-1}}]P_l^1(\cos\vartheta)e^{i\phi} = g(\vartheta)e^{i\phi}\end{aligned} \tag{2.17}$$

The solution of the scattering problem is then reduced to the calculation of the scattering phase η, which depends on the electron energy and on the scattering potential. An analogous calculation for the spin in the -*z* direction gives the S_{12} and the S_{22} amplitude.

$$\begin{aligned}S_{22} &= S_{11} = f(\vartheta) \\ S_{12} &= -S_{21}e^{-2i\phi} = -g(\vartheta)e^{-i\phi}\end{aligned} \tag{2.18}$$

From the superposition of the two bases solutions, with spin parallel and anti-parallel, the case for an electron with arbitrary spin direction can be worked out.

$$\begin{pmatrix} A \\ B \end{pmatrix} \exp(ikz) \tag{2.19}$$

Eq 2.19 is the wave function of the incident electron with A and B constant while the scattered asymptotic wave function is:

$$A\begin{pmatrix} S_{11} \\ S_{21} \end{pmatrix}\frac{\exp(ikr)}{r} + B\begin{pmatrix} S_{12} \\ S_{22} \end{pmatrix}\frac{e^{ikr}}{r} = \begin{pmatrix} Af - Bge^{-i\phi} \\ Bf + Age^{i\phi} \end{pmatrix}\frac{e^{ikr}}{r} = \begin{pmatrix} a_1' \\ a_2' \end{pmatrix}\frac{e^{ikr}}{r} \tag{2.20}$$

Using this last equation it is possible to calculate the differential cross section

$$\begin{aligned} &\frac{d\sigma}{d\Omega}(\vartheta,\phi) = \frac{|a_1'|^2 + |a_2'|^2}{|A|^2 + |B|^2} = \\ &= |f|^2 + |g|^2 + \frac{-AB^* e^{i\phi} + A^* B e^{-i\phi}}{|A|^2 + |B|^2}(fg^* - f^* g) \end{aligned} \tag{2.21}$$

By defining the Sherman function as

$$S(\vartheta) = i\frac{fg^* - f^* g}{|f|^2 + |g|^2} \tag{2.22}$$

the differential cross section becomes

$$\frac{d\sigma}{d\Omega}(\vartheta,\phi) = (|f|^2 + |g|^2)(1 + S(\vartheta)\frac{-AB^* e^{i\phi} + A^* B e^{-i\phi}}{i(|A|^2 + |B|^2)}) \tag{2.23}$$

By considering for example, *A=1* and *B=1*, *i.e.* an electron polarized in the *x* direction, the cross section results,

$$\frac{d\sigma}{d\Omega}(\vartheta,\phi) = (|f|^2 + |g|^2)(1 - S(\vartheta)\sin(\phi)) \tag{2.24}$$

therefore, there is a scattering asymmetry in the plane perpendicular to the propagation direction *z*. In conclusion an electron that hits the gold foil has different probability to be scattered in different directions. This is the principle of the Mott-scattering process. Important is to note that for a Mott detector with 4 plates for electron detection, the *x* and *y* polarization of the incident beam can be resolved.

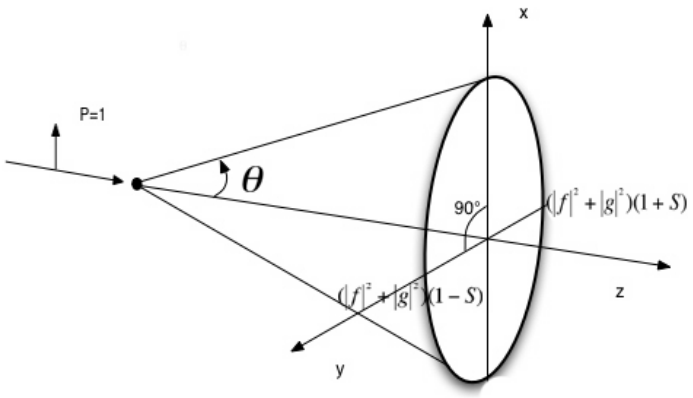


Fig 2.4. Left-right scattering asymmetry of a beam totally polarized in the *x* direction

From this formalism the Sherman function represents the spin sensitivity of the detector, *i.e.* the probability of scattering for polarized electron beams.

This treatment is referred to a system with one scattering centre. In reality for a gold foil (*i.e.* infinite scattering centres) the scattering asymmetry and the Sherman function are obtained through a more complex analysis.

2.5 Characterization of time resolution and energy resolutions for the ToF spectrometer

A ToF electron spectrometer is characterized by measuring its time and the energy resolutions. For the time resolution it is important to take into account the efficiency for a detectors to discriminate electrons collected at different times, (i.e. the minimum detector dead time) and the time needed by the electronics to digitalize the information and stop the clock. The total time resolution of the analyzer is measured by rotating the sample such that the specular reflection of the laser beam hits the gold foil of the Mott-polarimeter. In each of the four spectra acquired by the Mott-polarimeter used for the present experiment, a very narrow line at very short times is measured corresponding to the laser light diffused by the gold foil and detected. The overall time resolution is calculated by fitting this curve with a Gaussian function (Fig 2.5). Following this procedure the overall time resolution is found to be ~293 ps.

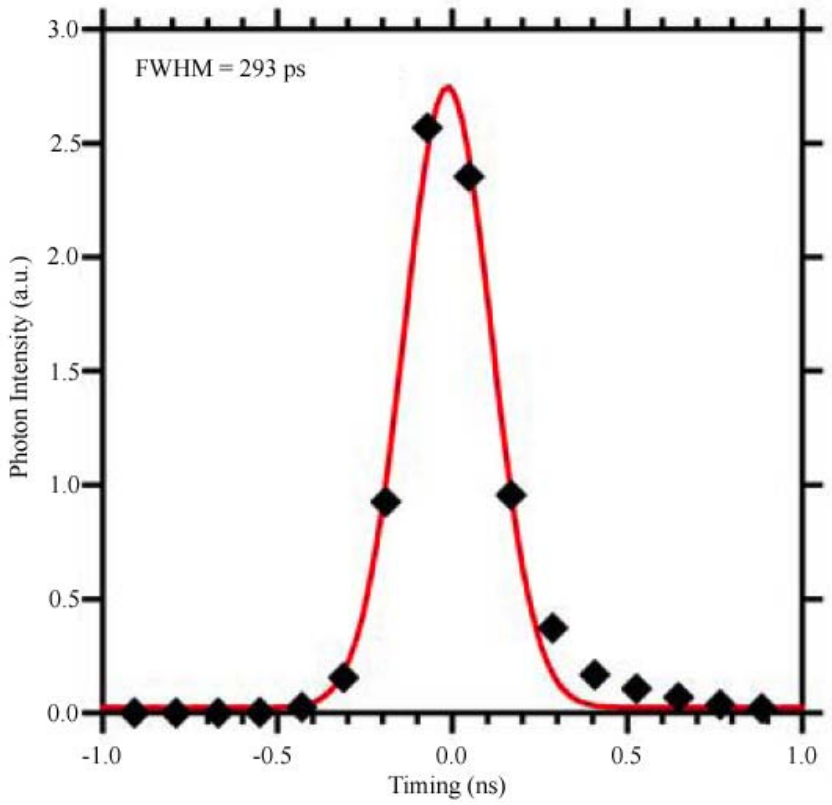


Fig 2.5. Characterization of the time resolution of the detector by measuring the photon diffused by the gold foil

The energy resolution of the analyzer is obtained from the measure of the spin integrated normal emission spectra (Fig 2.6). At normal emission (i.e. around the Γ point of the first Brillouin zone) the surface states overlap so the opposite spin states of the photoelectrons compensate while the main feature of the spectrum is the 92 meV wide surface states emission.

The Fermi edge is clearly detected and it can be fitted by a room temperature Fermi-Dirac function convoluted with a 28 meV Gaussian function (to take into account the thermal dispersion). It is also possible to see the 20 meV wide

cut off at zero kinetic energy. From this cut-off the energy resolution is estimated to be ~25 meV.

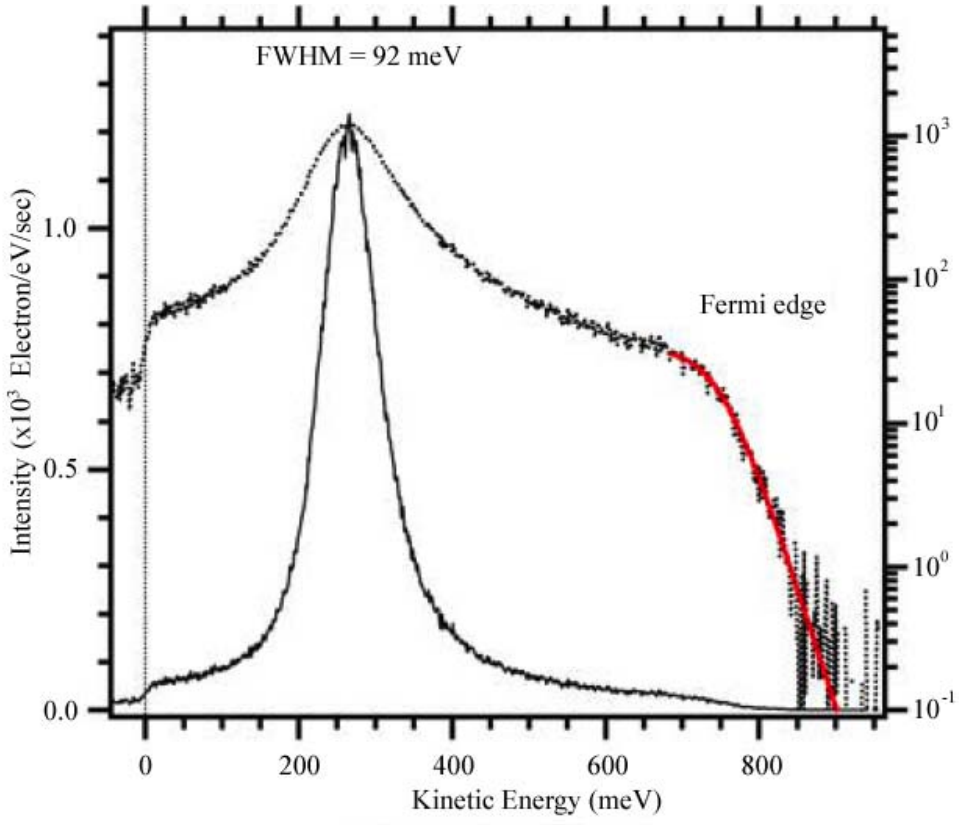


Fig 2.6 Spin integrated normal emission spectra in linear and logarithmic scale. The surface states width measured is 92meV while the Fermi edge is fitted by a Fermi-Dirac distribution convoluted with a 28meV width Gaussian function.

The Mott-detector and ToF calibration

In this section the procedure used to characterize the Time-of-Flight spin detector is described. As is reported in section 2 the 200 nm laser pulse is used to photoemit the electron from the Au(111) surface states. The first part describes the conversion of the raw data into spin data. Then the fitting procedure and the way to extract the spin asymmetry and the Sherman function are illustrated. In the last part the parameter of the Mott-detector are obtained as a function of the voltage applied between the two hemispheres. This procedure allows define the best operating condition.

3.1 Conversion of the raw data in spin data.

The measurement procedure consists in various scan at different angles of incidence (to span over different places of the reciprocal lattice) along the Γ-M direction of the reciprocal lattice. The sample is aligned whit the Γ-M direction along the horizontal axis. The surface states are fully polarized, because of this configuration the electrons are ejected with the tangential spin-polarization component along the vertical axis while the radial component should be along the horizontal direction, so the two vertical detectors should measure a little difference in the intensities at a given angle (off normal incidence) while the left right detectors should measure a bigger difference in the intensities at a given energy (off normal emission).

The electron distribution curve (EDC) of the four detectors is measured: the data acquired at an angle of –12.5° respect to the normal emission and at room temperature are shown in Fig 3.1.

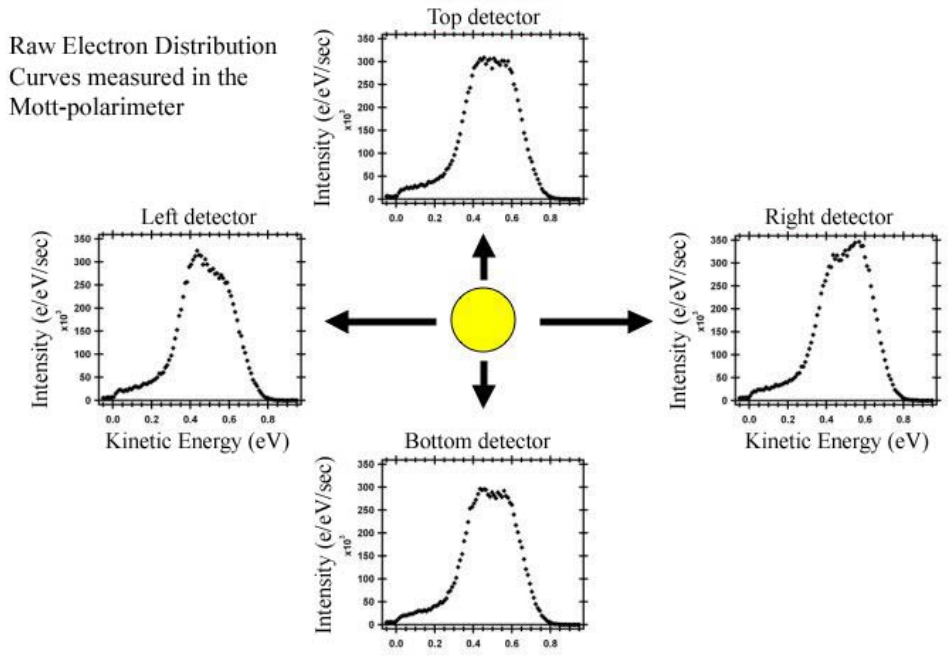


Fig 3.1 Presentation of the raw data obtained at –12.5°

From the figure 3.1 it is possible to notice that the difference between the top and the bottom detectors is small compared to the difference between the horizontal detectors. In order to obtain information about the spin of the surface states it is important to extract the polarization of the electrons beam as a function of the energy. By considering only the two horizontal detectors the two intensities can be written as:

$$I^L(E) = g_L \frac{N_0 \Omega}{2}(1 + P(E)S)$$
$$I^R(E) = g_R \frac{N_0 \Omega}{2}(1 - P(E)S) \qquad (3.1)$$

where g_R and g_L represent the right and left detectors parameter respectively, N_0 is the total number of electron emitted, Ω is the term that describes the

angular distribution of the electrons, $P(E)$ is the electrons beam spin-polarization function versus the electrons energy and S is the Sherman function. In the case of the eq 3.1 it is assumed that *spin up* electrons have a major probability to be scattered in the *left* direction. To find the number of electrons revealed with *spin up* ($N^{\uparrow}$) and *spin down* ($N^{\downarrow}$) at a given energy and angle, eq 3.1 can be re-written as

$$\begin{aligned} I^{L}(E) &= \alpha \frac{\tilde{N}_0}{2}(1+P(E)S) \\ I^{R}(E) &= \frac{\tilde{N}_0}{2}(1-P(E)S) \end{aligned} \qquad (3.2)$$

where $\tilde{N}_0 = g_R N_0 \Omega$ and $\alpha\tilde{N}_0 = g_L N_0 \Omega$ represent the effective number of electrons hitting the detectors, α represents the ratio between the parameter of the right and left detectors. Then the number of electrons with *spin up* and *spin down* is represented as

$$\begin{aligned} N^{\uparrow} &= \frac{\tilde{N}_0}{2}(1+P) \\ N^{\downarrow} &= \frac{\tilde{N}_0}{2}(1-P) \end{aligned} \qquad (3.3)$$

By combining the two formulas in eq 3.2 is possible to obtain $P(E)$ as

$$P(E) = \frac{1}{S}\frac{I^{L}-\alpha I^{R}}{I^{L}+\alpha I^{R}} \qquad (3.4)$$

A further parameter to be defined is the experimental asymmetry. This is the asymmetry detected by the Mott-polarimeter for an un-polarized electron beam $A_{exp} = \alpha - 1/\alpha + 1$ where α represent the ratio between the detectors parameters. The experimental asymmetry takes into account the effective difference between the two detectors efficiency induced by misalignment of the apparatus, size of the electrons beam etc. Using this definition

$$\alpha = \frac{1+A_{exp}}{1-A_{exp}} \qquad (3.5)$$

Instead the measured asymmetry that takes into account the physical asymmetry of the system is given by

$$A(E) = \frac{I^L(E) - I^R(E)}{I^L(E) + I^R(E)} \tag{3.6}$$

By substituting eq 3.5 and eq 3.6 into eq 3.4 the polarization function can be written as

$$P(E) = \frac{1}{S}\frac{A(E) - A_{\exp}}{1 - A(E)A_{\exp}} \tag{3.7}$$

From eq 3.7 is clear that the experimental asymmetry and the Sherman function must be evaluated to measure electron beam polarization.

3.2 Self calibration of the electron distribution curve (EDC), the experimental asymmetry and the Sherman function.

The experimental asymmetry and the Sherman function can be obtained from measured intensities of the horizontal detectors after some considerations.
Since surface states are fully spin polarized in the tangential direction with opposite spin, it is possible to assume $P_{SS1} = -P_{SS2} = 100\%$ where *SS1* is the *spin up* surface state and *SS2* is the *spin down* surface state. By dividing the two in eq 3.2 and substituting the expression in eq 3.5 the following relation is obtained

$$\frac{1-PS}{1+PS} = \frac{I^R}{I^L}\frac{1+A_{\exp}}{1-A_{\exp}} \tag{3.8}$$

Since the surface states have opposite spin ($P_{SS1} = -P_{SS2}$)

$$\frac{1-SP_{SS1}}{1+SP_{SS1}} = \frac{1+SP_{SS2}}{1-SP_{SS2}} = \left[\frac{1-SP_{SS2}}{1+SP_{SS2}}\right]^{-1} \tag{3.9}$$

while eq 3.8 results

$$\frac{I^R_{SS1}}{I^L_{SS1}}\frac{1+A_{\exp}}{1-A_{\exp}} = \left[\frac{I^R_{SS2}}{I^L_{SS2}}\frac{1+A_{\exp}}{1-A_{\exp}}\right]^{-1} \tag{3.10}$$

From the eq 3.10 is possible to extract of the experimental asymmetry as a function of the intensities detected by the two detectors for the two surface states (*SS1* and *SS2)*,

$$A_{\exp} = \frac{\sqrt{I^L_{SS1}I^L_{SS2}} - \sqrt{I^R_{SS1}I^R_{SS2}}}{\sqrt{I^L_{SS1}I^L_{SS2}} + \sqrt{I^R_{SS1}I^R_{SS2}}} \tag{3.11}$$

Since the surface states are fully spin polarized ($P_{SS1} = 100\% = 1$) the Sherman function is given by the following expression

$$S = \frac{\sqrt{I_{SS1}^{L} I_{SS2}^{R}} - \sqrt{I_{SS1}^{L} I_{SS2}^{R}}}{\sqrt{I_{SS1}^{L} I_{SS2}^{R}} + \sqrt{I_{SS1}^{L} I_{SS2}^{R}}} \qquad (3.12)$$

These two quantities can be directly deduced from the experimental data by a fitting procedure. In the following the procedure to extract the information from the Electron Distribution Curve (EDC) is presented along with the procedure to obtain from the spin polarization the pure spin data. It is worth to note that in the present case no retarding voltage was applied to the Time-of-Flight analyzer.

The first step of the analysis consists in finding the energy position of the surface states at a given angle. Since at room temperature the thermal broadening is larger than the energy splitting, a double Voigt fit with a flat background is applied to the spin integrated spectra (see Fig 3.2). The intensities and the widths of the two Voigt functions are chosen to be equal in order to set some constrains to the fitting process. Fig 3.2 presents the spin-integrated data in the kinetic energy region between 0-800 meV. A broad emission centred at ~500 meV below the Fermi energy is detected. This emission shows quite clearly two components that correspond to the two emissions from the surface states.

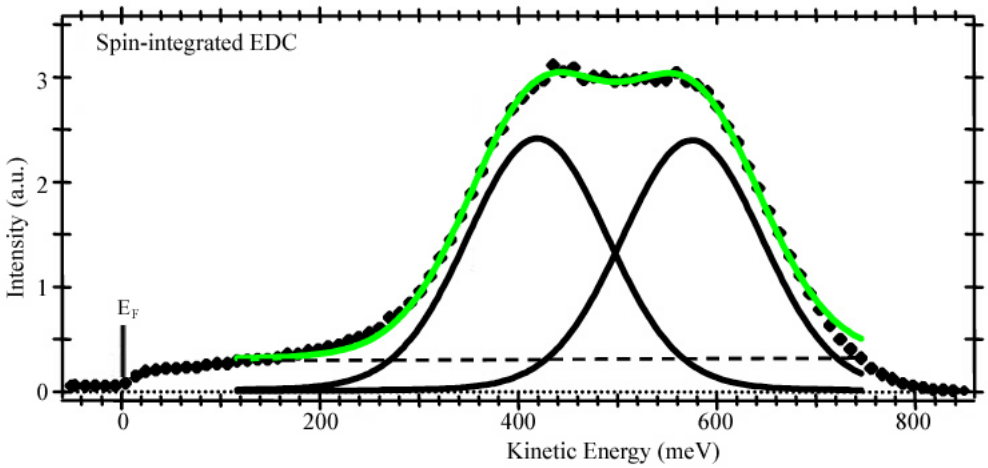


Fig 3.2. Spin integrated measure obtained by the average on the four detectors of the Mott-polarimeter (dots). The energy position and the width of the surface states are obtained by a double Voigt fitting (Black curves) with a flat background.

By decomposing these data with a double Voigt fitting it is possible to obtain the kinetic energy and the full width half maximum (FWHM) of the surface states. (*KE_{SS1}~ 575 meV, KE_{SS2} ~ 419 meV, $FWHM_{SS1}$ ~ 168 meV and $FWHM_{SS2}$ ~ 168meV)*

Also the emission intensities measured by each detector can be obtained by the double Voigt fitting procedure by subtraction of a flat background (see Fig 3.3). The energy values and the width are taken from the previous fit using as a free parameter the intensities of the two emissions. The signal intensities obtained (two for each detector corresponding at the *SS1* and *SS2*) are used to calculate the Sherman function and the experimental asymmetry. In the present case the values obtained are: $A_{\exp} = 2.6 \pm 0.2\%$ and $S = 10.8 \pm 0.7\%$

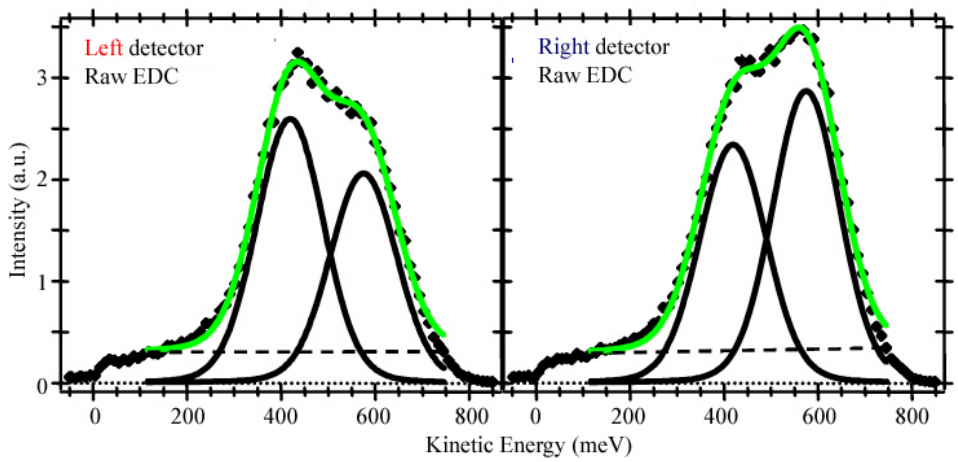


Fig 3.3. Left and right detectors fitted using the parameter from Fig 3.2; only the intensities of the surface states are free.

From these data and using eq 3.7 the spin resolved state could be obtained from

$$I_{\uparrow\downarrow}(E) = I(E)(1 \pm P(E)), \qquad (3.13)$$

where $I(E)$ is the intensities of the spin-integrated fitting (Fig 3.2).

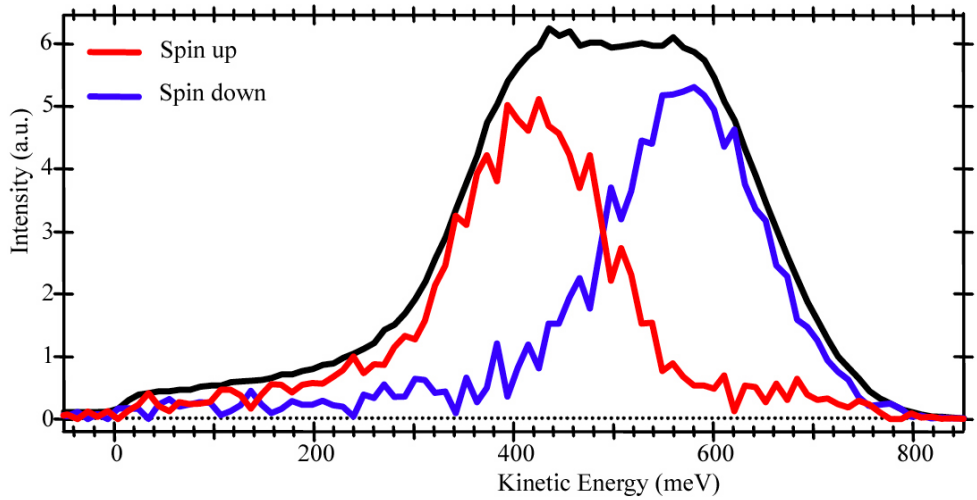


Fig 3.4 Spin resolved EDC (red and blue) curves obtained from the previous analysis. The black curve represents the sum of the two states.

Figure 3.4 shows that the surface states can be clearly resolved with a constant background. The FWHM of these states originates from the thermal broadening at room temperature. The symmetry in the noise indicates that the spin polarization $P(E)$ noise, resulting from the differential measurements between the two detectors, is predominant where compared to the $I(E)$ noise.

3.3 Sherman function versus the Mott-polarimeter high voltage scattering

The behaviour of the Mott-polarimeter strongly depends on the voltage applied between the two hemispheres. This characteristic is analyzed by calculating the Sherman function and the number of photoelectrons measured as a function of the accelerating voltage. This analysis is made at two emission angles (–12.5° and +12.5°) and for different voltages between 10 kV and 30 kV with step of 2 kV.

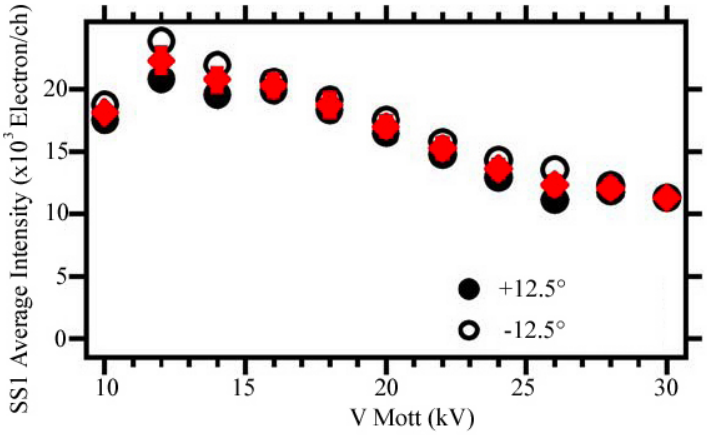


Fig 3.5. SS1 total intensity measured versus the high voltage applied to the Mott-detector. The measurements were performed at two angles: -12.5° (circle) and 12.5° (solid circle). The red diamonds represent the average intensity.

Fig 3.5 presents the intensities associated to the *SS1* as a function of the voltage applied between the Mott-polarimeter hemispheres. The data are presented for two emission angles ±12.5°. The average values and the error bars are obtained from the fitting parameters errors for an interval of confidence of 95%. It is possible to see that the number of the measured electrons decrease by rising the voltage. This is very likely due to the fact that by increasing the accelerating voltage the electrons enter deeper into the atomic shells of the gold

target of the Mott-polarimeter so the number of back elastic-scattered electrons decrease.

Fig 3.6 shows the variation of the Sherman function as a function of the high voltage.

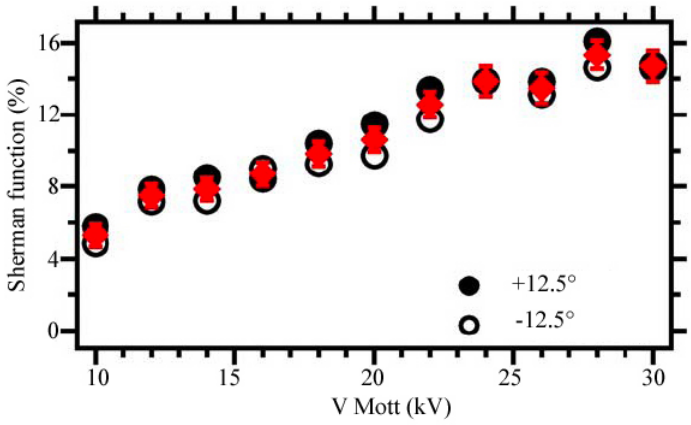


Fig 3.6 Sherman function as a function of the high voltage applied between the two hemispheres of the Mott-polarimeter. The circle refers to the measurement done at –12.5° while the solid circle refers to the measurement done at 12.5°. The red diamonds are the average Sherman function.

The Sherman function rises by increasing the accelerating voltage. This effect can be rationalized by considering that electrons at higher kinetic energy penetrate deeper in the gold electronic shells feeling a stronger gradient of the Coulomb potential. Since the spin-orbit interaction is proportional to the gradient of the Coulomb potential the Sherman function will increase by increasing the scattering electron kinetic energy.

By assuming a statistical origin ($\Delta I = \sqrt{I}$) for the noise component of the signal it is possible to find the best conditions for the analysis. Using eq. 3.7 and ignoring the systematic the errors on the polarization for a given values of the Sherman function can be estimated [22]

$$\Delta P = \frac{1}{S}\Delta A \qquad (3.14)$$

where ΔA is the error on the asymmetry defined in eq 3.6.

From the error propagation law, ΔA for the and relatively to the ΔI^R and ΔI^L statistical errors can be expressed as

$$\Delta A = \sqrt{\left(\frac{\partial A}{\partial I^L}\right)^2 (\Delta I^L)^2 + \left(\frac{\partial A}{\partial I^R}\right)^2 (\Delta I^R)^2} = \\ = \sqrt{\left(\frac{2I^R}{(I^R + I^L)^2}\right)^2 (I^L) + \left(\frac{-2I^L}{(I^R + I^L)^2}\right)^2 (I^R)} \tag{3.15}$$

By setting $I = I^R + I^L$,

$$\Delta A = \sqrt{\frac{4I^R I^L}{I^3}} \tag{3.16}$$

Finally by ignoring the experimental asymmetry it is possible to obtain

$$P = \frac{1}{S}\frac{I^L - I^R}{I^L + I^R}$$

$$1 - P^2 S^2 = \frac{4I^L I^R}{I^2} \tag{3.17}$$

By substituting eq 3.17 in eq 3.16 $\Delta A = \sqrt{\frac{1}{I}(1 - P^2 S^2)}$ and

$$\Delta P = \sqrt{\frac{1}{I}\left(\frac{1}{S^2} - P^2\right)}. \tag{3.18}$$

In real Mott-detectors the Sherman function is not very large so it is possible to neglect the second power of the polarization term in eq 3.18. Under this conditions

$$\Delta P = \sqrt{\frac{1}{IS^2}} \tag{3.18).}$$

The quantity IS^2 must then be maximized to have the minimum error on the spin polarization. This result is regarded as the figure of merit (FOM) for the Mott-polarimeter. Fig 3.7 shows the behaviour of the FOM as a function of the high voltage applied between the two hemispheres of the Mott-polarimeter.

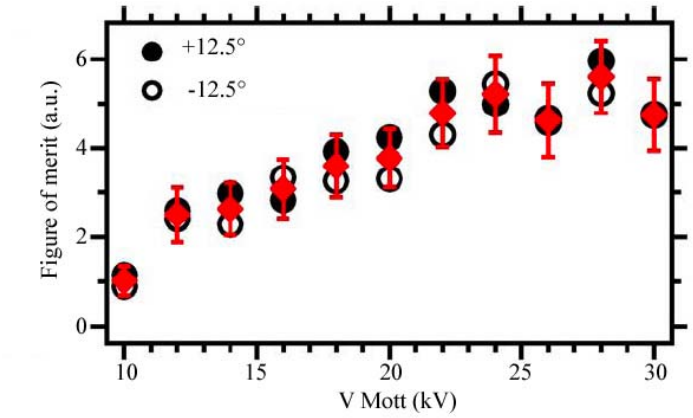


Fig 3.7 The Figure of merit increases with the high voltage until it reaches a plateau at 25 kV

Figure 3.7 shows a rise of the FOM, for increasing the accelerating voltage, up to 25 kV where a flat plateau starts. In particular, from Fig 3.5 and Fig 3.6 it is possible to see that while the surface states intensity decrease by ~50% with the voltage, the Sherman function rise by ~300%.

From this analysis it is possible to conclude that the best operative condition, in terms of spin detection efficiency, are found for accelerating voltage between 25 kV and 30 kV.

Spin resolved photoemission from the Au(111) surface states.

This section presents the data on the energy dispersion of the surface states. All measurements were performed at room temperature and with no retarding potential applied to the Time-of-Flight analyzer. The voltage applied between the two hemispheres of the Mott-polarimeter was 25kV. An attempt to measure the radial component of the spin polarization is also presented. The presence of the radial component in the spin polarization is predicted by DFT calculations [8] that suggest the presence of a small component of the spin in the horizontal plane (along $\bar{\Gamma}$-M). The vertical detectors of the Mott-polarimeter should reveal this component.

4.1 Angular dispersion of the surface states.

The spin-integrated data between ±22° are reported in the left panel of Fig 4.1. The kinetic energy of the electrons are reported as a function of the reciprocal parallel wave vector, while the sum of the intensities, as measured by the four detectors, are represented in a colour scale. In the left panel of Fig 4.1 it is clearly visible the parabolic shape of the energy dispersion of the surface states.

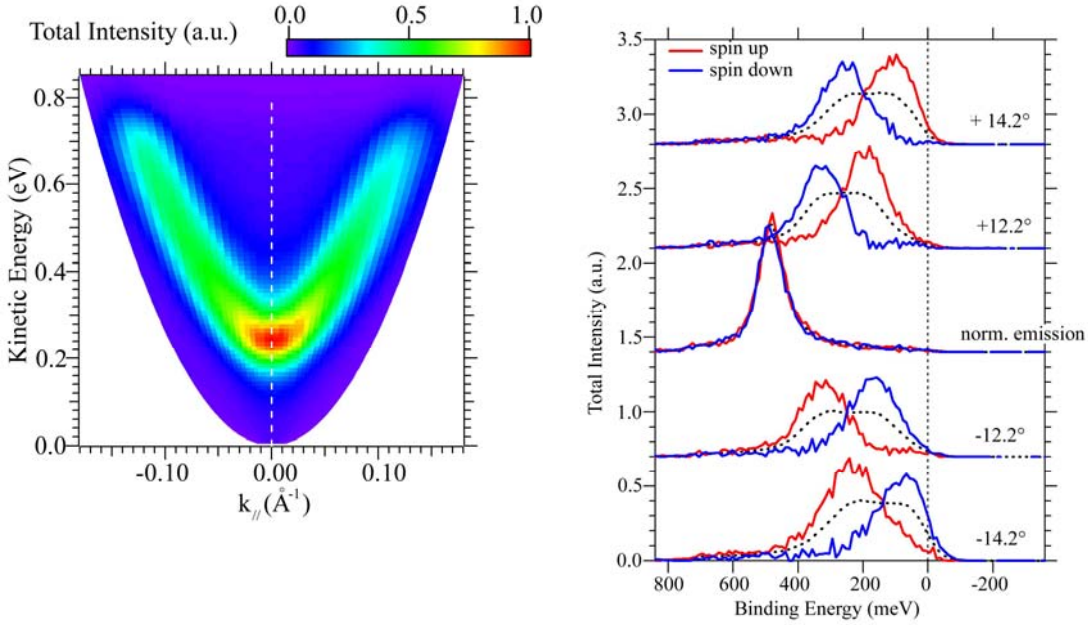


Fig 4.1 Left panel: Spin integrated data at a given values of the reciprocal parallel momentum and at a given kinetic energy, the sum of the four intensities measured by the detectors is represented in a colour scale. Right panel: Spin resolved data of the two surface states at different angle of incidence of the light considering the left-right detectors. The red curve is the *spin up* state while the blue curve is the *spin down* state. The dots curve is the spin-integrated signal.

The right panel of the Fig 4.1 shows the pure spin intensities derived from the data using the procedure reported in section 3 for the left-right detectors. The spin resolved states are reported for different emission angles between $\pm 12.5°$. At normal emission the two surface states are superimposed in agreement with the theory. By changing the angle, and so the values of $\bar{k}_{//}$ respect to the surface, the binding energy changes and the splitting between the two states appears. What is also changing is the respective position of the states. For positive angle the *spin up* state has a lower binding energy with respect the *spin down* state and opposite for negative angles.

The peaks in the right panel of Fig 4.1 represent the binding energy of the surface states at a given angle of incidence, so at a given value of $\bar{k}_{//}$.

Collecting the intensities at all possible angles it is possible to have the energy dispersion of the surface states, so their binding energy (or their kinetic energy which is $E_{kin} = h\nu - E_B - \phi$, where $h\nu$ is the photon energy, E_B is the binding energy relative to the Fermi energy and ϕ is the work function of the sample) as a function of $\bar{k}_{//}$. For simplicity in the following all the photoelectrons emissions are reported versus the photoelectron kinetic energy.

Once the spin polarization is measured it is possible to find the number of electrons with *spin up* and the number of electrons with *spin down* (see section 3) in the tangential direction. The number of electrons with *spin up* is then subtracted from the number of electrons with *spin down* to obtain a *spin up – spin down* differential distribution map. Fig 4.2 shows the results of this analysis at a given angle of incidence considering the vertical difference, *i.e.* the difference of polarization into the tangential component. The same is done considering the horizontal difference, *i.e.* for the radial component. The Sherman function obtained from the analysis of the left-right detectors measurements is used also for the analysis of the radial component. The experimental asymmetry cannot be calculated from the data acquired with the

top-bottom detectors because, as it is explained in chapter one, the surface states are not fully polarized into the radial component and their polarization is not opposite. Therefore the experimental asymmetry is taken as a fitting parameter for the analysis of the radial component.

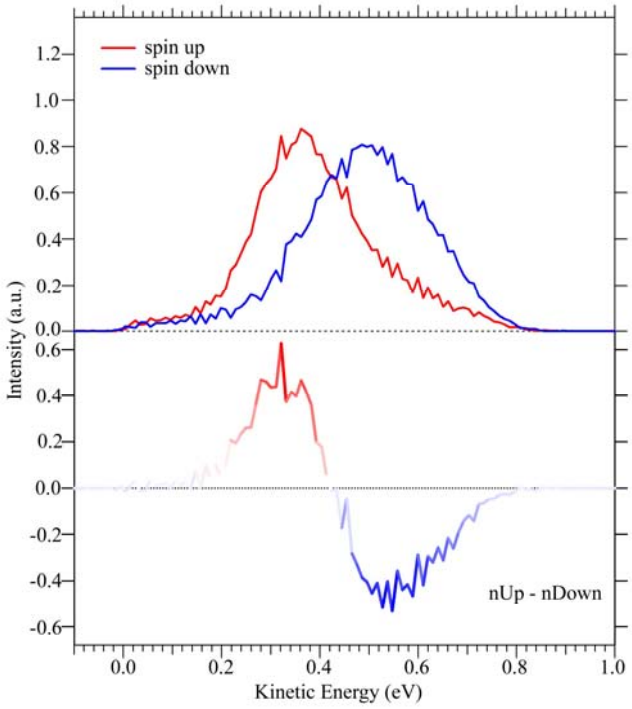
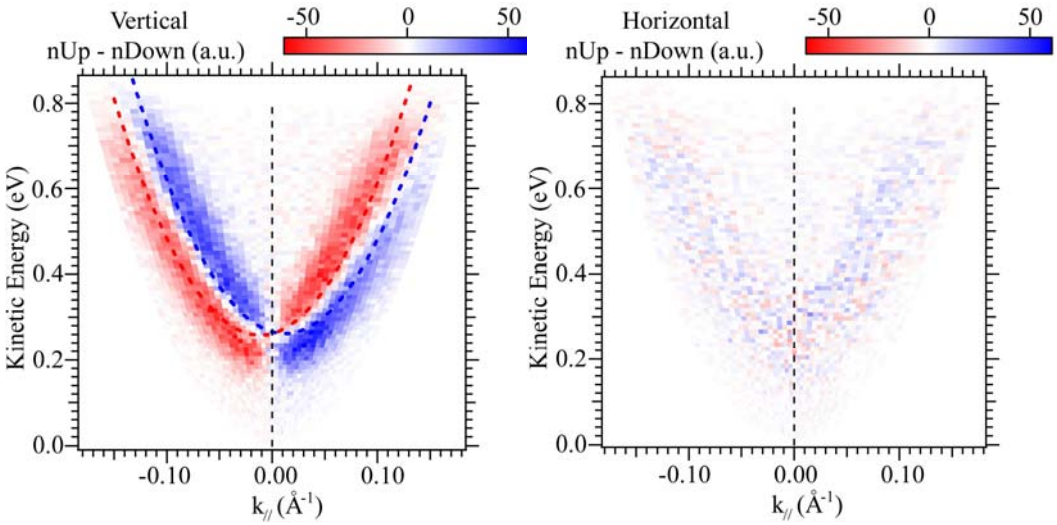


Fig 4.2: Top: the pure spin data at a given angle of incidence, the red curve represent the *spin up* while the blue curve represent the *spin down.* Down: subtraction of the spin data $(n_{\uparrow} - n_{\downarrow})$ at a given angle.

Performing this kind of subtraction between the number of electrons detected from the four detectors and considering the difference in the vertical direction (tangential component of spin polarization using the values extracted from the measurements done by the left-right detectors) and in the horizontal direction (radial component of spin polarization using the values extracted from the measurements done by the up-down detectors) the spin-split maps of the surface states are obtained. Fig 4.3 shows the difference between the numbers of *spin-up* and the *spin-down* electrons in the horizontal and vertical directions

at a given kinetic energy of the photoelectrons and at a given value of the reciprocal parallel momentum vector.



.

Fig 4.3 Maps of the surface states taking into account the spin-split. Left: Vertical difference (tangential component). Right: Horizontal difference (radial component), the dots curve are derived from the fitting on the energy dispersion of the surface states.

In the vertical direction is clearly visible the spin splitting of the two surface states, while in the horizontal direction this difference is less evident. For the vertical directions one can easily distinguish the two different parabolic distributions of the surface states. Near the Γ point there is a white vertical strip indicating that the two states have the same binding energy for normal emission.

For the horizontal direction is very difficult to see the different distributions of the two parabolas. The right panel of the figure 4.3 seems to be only noise. In fact, near the Γ point is also present the colour difference, which is comparable with the other part of the figure.

Now it is possible to consider one surface state at time. In particular, considering the positions of each maximum for a single surface state, at a given value of the reciprocal parallel lattice vector, it is possible to extract the energy dispersion of the two surface states once at a time.

This dispersion can be fitted for each surface state by a parabola with the minimum out of $k_{//} = 0$. The fitted equation is $E_{\pm} = E_0 + \frac{\hbar^2}{2m^*}(|k_{//}| \pm k_0)^2$ where m^* is the effective mass of the surface states electrons, k_0 is the momentum value corresponding to the parabola minimum and the + (-) refers to the state with *spin up* (*spin down)*. The displacement from $k_{//} = 0$ should be equal, in absolute value, for the two surface states.

Fig 4.4 shows the fitting of the energy dispersion of the two surface states.

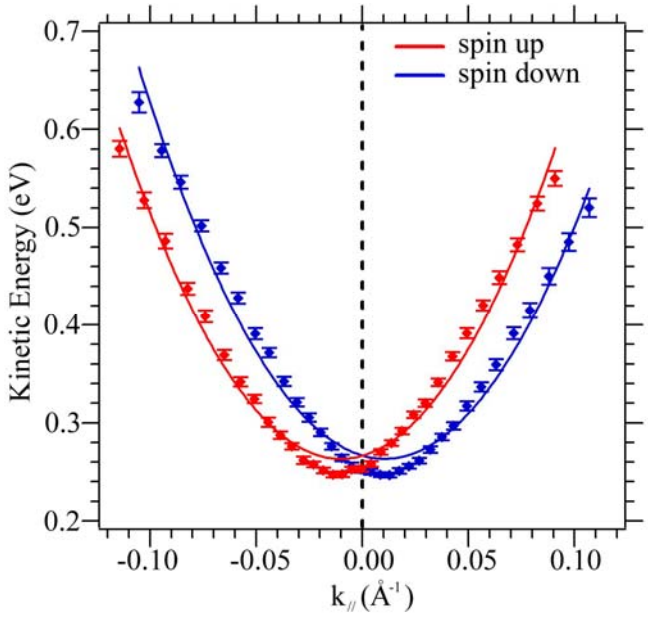


Fig 4.4. Fit of the surface states energy dispersion

All points are plotted with an error extracted from the fitting procedure errors and with an interval of confidence of ~ 95%.

The values obtained from this fit are: $E_0 = 260\ meV$, $m^* = 0.134\ m_e$, $k_0 = 0.011 Å^{-1}$ for each of the two fits. The distance between the minima of the two surface states is $2k_0 = 0.022\ Å^{-1}$ well agrees with the theoretical value of $0.023 Å^{-1}$, obtained from DFT calculations [8]. The effective mass, instead, is lower than the theoretical one (0.20 m_e) and also lower than what calculated from others groups (0.25 m_e) [4], [8].

It is important to notice that the values of the effective mass and the displacement of the minimum of the bands from $k_{//} = 0$ are equal, for the two surface states, within the resolution of the instruments.

Another important point is that the interval of confidence of 95% of the minima of the two bands is 2 meV.

4.2 Attempt to measure the radial spin component

The binding energy of the two surface states was also investigated by changing the azimuth angle ϕ (rotating the sample with respects an axis perpendicular to the surface) at a given value of polar angle θ of –12.5°. The binding energy of the two surface states should remain the same changing ϕ, as reported before. Fig 4.5 shows the results of this analysis using the tangential component. For each of the data reported in Fig 4.5 the Sherman function and the experimental asymmetry were calculated following the procedure reported before.

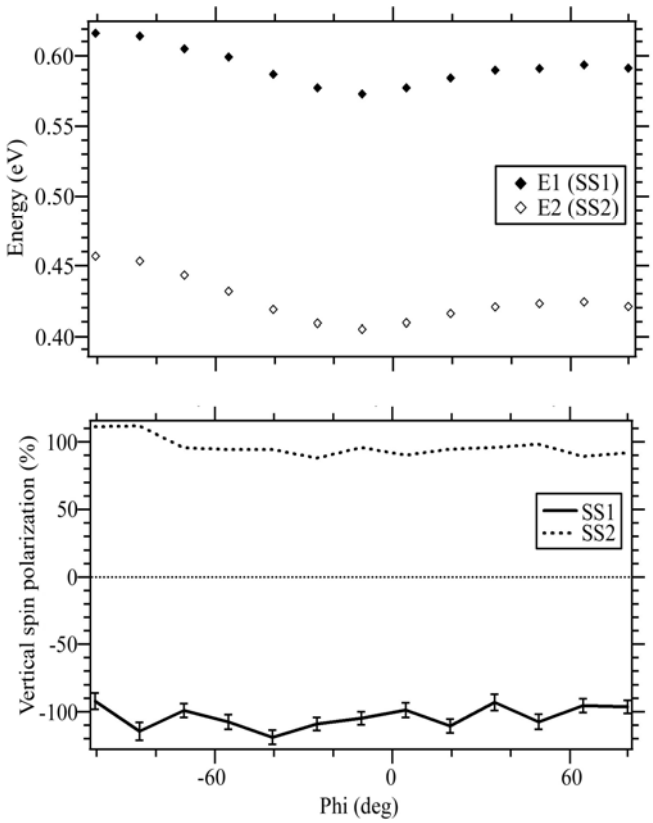


Fig 4.5: Top panel: Binding energy of the two surface states as a function of the azimuth angle ϕ. Bottom panel: Spin polarization of the two surface states as a function of the azimuth angle ϕ, the error bars are showed only for one state because are the same for the other one.

The first panel of Fig 4.5 shows the binding energy of the two surface states as a function of ϕ. The binding energy of the two states varies in the same way keeping equal the energy distance from them.

This suggests that the kinetic energy of the electrons measured changes ϕ and the electrons take different time to travel from the sample to the detectors. This difference could originate from non-homogeneity of the system, due to uncontrolled mechanical movement or uncontrolled background electric or magnetic field.

Effects due to uncontrolled background electric or magnetic field are shown in Fig 4.6. For the first case it is assumed that the electrons enter into the Time-of-Flight with a linear trajectory (blue line), while for the second case electrons with a different emission angle follow a perturbed trajectory and they are collected in the ToF as the electrons of the straight trajectory. This happened for both *spin up* and *spin down* electrons keeping the binding energy difference of the two surface states fixed.

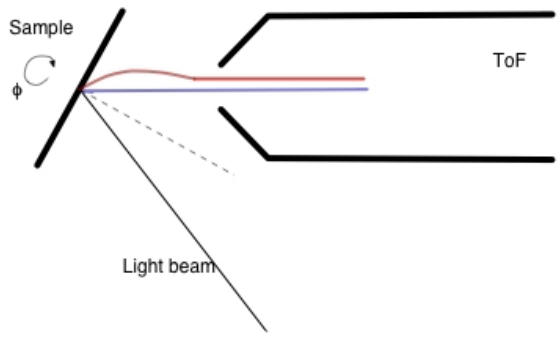


Fig 4.6 Schematic view of the mechanism that brings the binding energy difference at each azimuth angle for the two surface states. The coloured line corresponds to electrons emitted at different azimuth angle.

The bottom panel of Fig 4.5 shows the vertical spin polarization, *i.e.* the tangential spin polarization, of the two surface states; the error bars are shown only for one of the two spin-polarization (they are equal for the two states). It is clearly visible that the tangential spin polarization is close to 100%, in absolute value, for each azimuth angle and for both surface states, as expected from the theory.

The behaviour of the radial component of the spin polarizations as a function of the azimuth angle is also calculated. Fig 4.7 shows this analysis. The error bars are reported only for one surface states (are equal for the two states), with an interval of confidence of 95%. The red lines represent the calculated values of the radial component [8], dots line for the surface state 2 (less polarized) and solid line for the surface state 1 (more polarized).

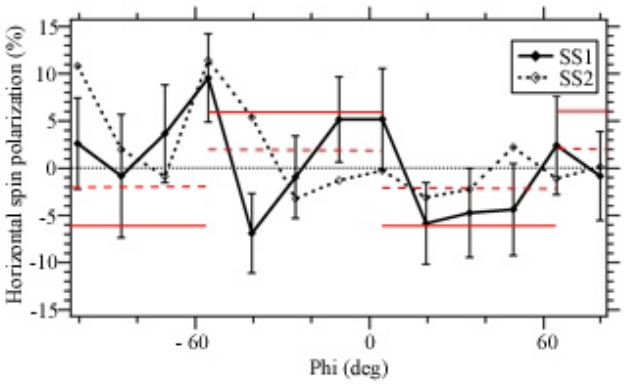


Fig 4.7 Radial component of the spin polarization of the two surface states as a function of the azimuth angle ϕ. The red lines represent the theoretical values: dots line for the SS2 and the solid line for the SS1.

This analysis shows that the radial component of the spin polarization has a high error bars compared to the values calculated. It is impossible to estimate properly the behaviour of the radial component of the spin polarization. The non-homogeneity of the system that brings different values of binding energy at each azimuth angle affects also the analysis on the radial component producing sometimes, ambiguous data. This problem is more evident for the measure of the radial component where the precision requirement is high.

This problem should be reduced by a new sample holder with a more accurate mechanism and proper materials to reduce the electrostatic background on the azimuth angle. The other problems due to the high error bars can be solved by decrease the temperature to reduce the thermal fluctuation and reduce the errors on the energy measured.

In this way the measurements of the radial component of the spin polarization should be achieved.

Conclusion

This thesis reports an angle and spin resolved photoemission spectroscopy study of the Au(111) surface state along the Γ-M direction. These states are formed by electrons trapped between the vacuum energy barrier and the bulk band-gap, the resulting two-dimensionality of the surface states leads to the rise of the *Rashba-Bychkov* interaction which brings the states to exhibit a spin-splitting originating from the spin-orbit interaction. This is the same mechanism present in the semiconductor heterojunctions where spin-orbit interaction is present.

The spin-polarization of the surface states can be divided into tangential and radial component with respect to the electrons distribution at a given energy in the reciprocal lattice. In fact, the surface states momentum dispersion in the surface Brillouin zone, at a given energy, is formed by two concentric circles with opposite spin. From DFT calculations it turned out that the tangential component of the surface states should be fully polarized with opposite values for the two states. This polarization component was well measured in previous works. Instead the radial component has the same sign for the two states, but

different absolute values (smaller than the tangential component) and changes sign every 60° in the plane of the surface. This component was not measured.

The experiment is performed using a Time-of-Flight analyzer coupled with a Mott-detector with four micro channel plates to resolve the spin in both directions parallel to the surface of the sample. The light source is the fourth harmonic of a Ti:Sa amplified laser (200 nm) with a repetition rate of 250 kHz.

The thesis reports also the characterization of the Time-of-Flight and the Mott-detector making use of the well-known character of the spin-polarization properties of the surface states. The full polarization of the tangential component of the surface states is used to derive the Sherman function and the experimental asymmetry of the Mott-detector.

The properties of the detector are also studied as a function of its parameter finding that the spin sensitivity depends strongly from the voltage applied between the two hemispheres of the Mott-detector. In particular changing the voltage from 10 to 25 kV the Sherman function rise about 300%; this is directly linked to the capability of the detector to distinguish the different spin orientation.

The spin resolved data and the energy dispersion of the two surface states are obtained using the Sherman function and the experimental asymmetry. The parallel reciprocal momentum distance, between the two states, are found to be $\Delta k_{//} = 0.022 Å^{-1}$, and in agreement with the theoretical calculations ($\Delta k_{//} = 0.023 Å^{-1}$) and previous experiment ($\Delta k_{//} = 0.026 Å^{-1}$) [4], [8]. The energy precision in the bottom of the energy distribution is ~2 meV. Instead the calculated effective mass of the surface states is lower ($m^* = 0.134 m_e$) than the predicted one ($m^* = 0.20 m_e$) and the effective mass found in previous experiment ($m^* = 0.25 m_e$).

The energy splitting of the surface states of other noble metals is week than in the Au(111), but decreasing the temperature of the system the error bars on the

spin polarization should be strongly reduced while the high precision of our experiment should allow to separate the spin components of surface states in metals with a smaller spin-orbit coupling energy, *i. e.* Cu and Ag for example.
Here it is also presented an attempt to measure the radial component of the spin polarization. This measure is very difficult because of the very value of the spin polarization in the radial direction (predicted as 6% for 0.17 eV binding energy for the most polarized state). The radial component of the spin polarization has the same sign for the two surface states but different values and it changes sign every 60° in the plane of the surface [8]. Due to this last property the radial component is investigated keeping fixed the angle of incidence of the light on the sample (*i. e.* the values of the reciprocal parallel momentum vector) and rotating the sample around an axis orthogonal to the surface. It turns out that the binding energy of the two surface states changes with this rotation. This can be due to the presence of a little electric field near the sample that changes direction as the sample is rotated. The electrons make a different path for each angle changing their time to reach the detectors. These oscillations in the binding energy are transferred to the calculation of spin polarization both tangential and radial component. The two components of the spin polarization oscillate for an absolute values around 10%. Another problem for measuring the radial component of the spin in surface states it is the quite large errors bars. This last problem can be solved decreasing the temperature of the system, while the problem on the binding energy oscillations can be solves making a new sample holder, more symmetric in order to keep the electrostatic background constant at each angle.

Bibliography

[1] W. Shockley, Phys. Rev. **56**, 317-23 (1939).

[2] S. G. Davison and M. Stéçlicka, *Basic Theory of Surface States* (Oxford: Oxford University Press 1992).

[3] E. Bertel and M. Donald, *Electronic Surface and Interface States on Metallic Systems* (Singapore: World Scientific 1994).

[4] F. Reinert, J. Phys: Condens Matter **15,** S693-S705 (2003).

[5] J. F. Janak, Phys. Rev. **178**, 1416 (1969)

[6] E. I. Rashba, Sov. Phys.-Solid State **2**, 1109 (1960).

[7] Y. A. Bychkov and E. I. Rashba, Sov. Phys.-JETP Lett. **39**, 78 (1984).

[8] J. Henk, M. Hoesch, J. Osterwalder, A. Ernst and P. Bruno, J. Phys: Condens. Matter **16**, 7581-7597 (2004).

[9] M. Hochstrasser, J. G. Tobin, E. Rotemberg and S. D. Kevan, Phys. Rev. Lett. **89**, 216802 (2002).

[10] S. Houfner, *Photoelectron Spectroscopy* (Springer-Verlag, Berlin Heidelberg, 2003).

[11] N. W. Ashcroft and N. D. Mermin, *Solid State Physiscs* (Holt, Rinehart and Winston, New York, 1976).

[12] **http://www.phys.ufl.edu/fermisurface/**

[13] L. Petersen, P. Hedegård, Surf. Sci. **459**, 49-56 (2000)

[14] P. O. Gartland and B. J. Slagsvold, Phys. Rev. B **12**, 4047 (1975).

[15] P. Heimann, H. Neddermeyer and H. F. Roloff, J. Phys. C: Solid State Phys **10**, L17-21 (1977).

[16] S. D. Kevan, Phys. Rev. Lett. **50**, 526-529 (1983).

[17]S. D. Kevan, Phys. Rev. B **33**, 4364 (1986)

[18]R. Matzdorf and A. Goldmann, Surf. Sci. **359**, 77 (1996)

[19]A. Beckmann, K. Meinel, Ch. Ammer, M. Heiler and H. Neddermeyer, Surf. Sci. **375**, L363 (1997)

[20] S. LaShell, E. Jensen and B. A. McDougall, Phys. Rev. Lett. **77**, 3419-3422 (1996).

[21] G. Nicolay, F. Reinert, S. Schmidt, D. Ehm, P. Steiner and S. Hüfner, Phys. Rev. B **62**, 1631-1634 (2000)

[22] K. S. Karlsson, G. Chiaia and U. O. Karlsson, Rev Sci Instrum **67,** 3610 (1996)

[23] L. Moreschini, G. Ghiringhelli, K. Larsson, U. Veit and N. B. Brookes, Rev. Sci. Instrum. **79**, 033905 (2008)

[24] J. Kessler, *Polarized Electrons* (Springer-Verlag, Berlin Heidelberg, (1976).

[25] L. I. Schiff, *Quantum mechanics*, 3rd ed. (McGraw-Hill, New York 1968)

[26] N. F. Mott and H. S. W. Massey, *The Theory of Atomic Collisions* (Clarendon, Oxford 1965) Chap. IX.